

Grooving and Doping by Laser Chemical Processing (LCP) for Silicon Photovoltaics

Tesi di L.S. in Ingegneria dei Materiali di:

Erika Biserni

(matr.734742)

Facoltà di Ingegneria dei Processi Industriali

AA 2009/2010

Lavoro svolto nell'ambito della collaborazione con il
Fraunhofer Institute for Solar Energy systems (ISE)

Freiburg, Germany

Relatore: Prof. A. Li Bassi
Supervisor@Fraunhofer ISE: Dr.A.Fell

Abstract

Laser Chemical Processing is a technique based on a laser beam coupled into a thin liquid jet (50 – 100 μm diameter), which was developed in 2003 at the Fraunhofer Institute for Solar Energy Systems (ISE) on the basis of the LaserMicroJetTM[27, 28, 23] by Synova S.A.

The use of a chemical solutions enables to induce combined thermal, fluid dynamic and chemical effects on the target surface, which possible applications in photo-voltaics range from silicon microstructuring to ingot wafering. Among those, Laser Chemical Processing has been used, i.e. to cut silicon with water as a liquid jet [21] or, on the other hand, to selectively dope silicon surface with a suitable dopant solution as a liquid jet[?, 20], resulting in shallow structures, up to depths of about 5 μm .

This thesis work deals with the possibility to exploit the Laser Chemical Processing for silicon wafers deep structuring and doping in just one process step.

The methodological approach has been to separately analyse each of the two main processes, that is, deep grooving and doping, aiming to enhance understanding of the effects in each involved by correlating results to the process parameters.

First, the dependence of grooves depth and quality on process parameters was studied, using water as a waveguide and a green laser system (532 nm) and optimizing the process for the 150 μm depth. While deep grooving, a problem had to be faced. In most cases, the obtained grooves were not continuous, showing some periodical interruptions. Then, a systematic study of the influence of the main parameters on the interruptions was carried out.

Secondly, a detailed study on shallower grooves, which are n^{++} doped by means of a phosphoric acid solution as a waveguide, was performed, mainly focusing on whether the doping can effectively shield the laser-induced damage.

Suitable characterizing tools have been used, ranging from microscopy to specially designed photoconductance measurements. LEXT confocal microscope was used to

image the grooves and measure their depth and other geometrical parameters. SEM images were also taken, to have a clearer image of groove interruptions. In order to evaluate the impact of laser damage on minority carriers lifetime after LCP with phosphoric acid, QSSPC (quasi-steady-state photoconductance decay) measurements were carried out. QSSPC measurement found also an interesting application in a special technique, designed and theoretically described by Fischer and Plagwitz, which was used to evaluate the surface recombination velocity of LCP grooves.

Estratto in lingua italiana

Questo lavoro di tesi è il frutto dell'attività svolta dall'autrice durante una collaborazione durata nove mesi con il gruppo di ricerca MLV, diretto da Filip Granek, presso il Fraunhofer Institute for Solar Energy systems (ISE) di Freiburg, Germania.

Tale attività si inserisce nel contesto della ricerca nel campo fotovoltaico e in particolare delle celle solari basate sul silicio.

L'argomento di questo lavoro è l'investigazione delle potenzialità di sviluppo di una tecnologia sviluppata nel 2003 al Fraunhofer ISE, basata sull'accoppiamento di un fascio laser in una guida d'onda liquida: il Laser Chemical Processing (LCP). Il getto liquido è ottenuto tramite pompaggio di acqua o soluzioni chimiche attraverso un ugello appositamente disegnato, con un'apertura di diametro variabile tra i 50 e i 100 μm , il quale, per mezzo di una finestra di vetro, consente l'accoppiamento del fascio laser nel getto, che agisce da guida d'onda. L'utilizzo di opportune soluzioni chimiche come mezzo liquido può essere sfruttato per indurre reazioni chimiche e fisiche nel bersaglio di silicio, come ad esempio il drogaggio selettivo tramite acido fosforico. Le applicazioni del LCP sono molteplici, dal *wafering* che promette una minore perdita di silicio sia durante il taglio del lingotto, sia nel rendere non necessarie le molteplici lavorazioni di pulitura e lucidatura richieste dal *multi-wire* (MSWT), all'apertura dello strato di passivazione per consentire la successiva metallizzazione, all'introduzione selettiva di drogante necessaria per ottenere il *selective emitter* caratteristico dei designs ad alta efficienza.

Il drogaggio selettivo tramite LCP avviene per fusione del silicio e successiva ricristallizzazione; nel silicio fuso, infatti, il fosforo ha un coefficiente di diffusione molto più elevato che nel silicio solido (ordini di grandezza) e pertanto diffonde durante tutta la vita del fuso. Il lento raffreddamento consente poi la solidificazione in forma cristallina del silicio nel quale è stato introdotto il drogante. Allo stato dell'arte, il drogaggio tramite LCP ha riguardato solo strutture superficiali, di profondità inferiori ai 5 μm . D'altra parte, il LCP è utilizzato, con acqua o soluzioni al cloro come mezzo liquido, anche per generare strutture tridimensionali, ovvero scavare *grooves*, la cui

utilità è sfruttata ad esempio nelle celle di tipo *Buried contact* o *Back contact*. La possibilità di unire queste due capacità del LCP per creare microstrutture tridimensionali nel wafer contestualmente al drogaggio selettivo è di indubbio interesse ma finora non è stata mai sondata.

Questo lavoro di tesi si pone appunto come obiettivo l'indagine di questo potenziale, partendo dall'analisi sistematica di alcune criticità dell'uno e dell'altro processo.

L'approccio seguito è stato quello di separare l'indagine in due principali momenti.

Inizialmente, si è studiato l'effetto dei parametri di processo sulla profondità e la qualità dei *grooves*, con la finalità di migliorare la comprensione dei complessi fenomeni ottici, termodinamici e fluidodinamici coinvolti e della loro interazione. In questa fase, nella quale un ampio intervallo di profondità è stato investigato ($20 \div 250\mu m$) tramite un laser verde ($532nm$, durata dell'impulso $\sim 400nm$), un inaspettato effetto è stato osservato: in alcuni casi i *grooves* apparivano non continui nella direzione della loro lunghezza, presentando interruzioni periodiche con cross-section a forma di dente di sega. La probabilità delle interruzioni è stata quindi analizzata in relazione ai parametri di processo.

In seguito, è stata indagata la possibilità di generare *grooves* dalle pareti drogate attraverso un processo con acido fosforico. Due diversi sistemi laser nel verde sono stati impiegati, ciascuno con un diverso range di durata dell'impulso ($\sim 10nm$; $\sim 400nm$). La "qualità" del risultato ottenuto è stata valutata in termini di velocità di ricombinazione superficiale (SRV) dei portatori di carica, ottenuta da misure di tempo di vita (QSSPC) tramite un modello teorico e un protocollo di misura appositi (Fischer/Plagwitz model). Sulla base del precedente studio sulla geometria dei *grooves*, sono stati scelti dei set di parametri che dessero sempre la stessa geometria del groove, in modo da poter trascurare l'influenza della maggiore o minore superficie non passivata generata. La diversa velocità di ricombinazione superficiale è, quindi, da un lato aumentata da un maggior danneggiamento indotto dal laser e dall'altro "schermata" dal doping introdotto (field effect passivation).

I risultati ottenuti nel regime di impulsi lunghi è promettente, offrendo valori di SRV assolutamente compatibili con la applicazione alle celle solari.

Contents

1	Introduction	13
1.1	Silicon Solar Cells	13
1.1.1	Losses	15
1.1.1.1	Optical losses	15
1.1.1.2	Recombination losses	16
1.1.1.3	Resistance and shunt losses	17
1.1.2	High efficiency concepts	18
1.1.2.1	PERL (Passivated Emitter Rear Locally diffused)	19
1.1.2.2	Back Contact solar cells	19
1.2	Laser Chemical Processing (LCP)	20
1.2.1	Physical effects in LCP	22
1.2.1.1	From nozzle exit plane to the target surface	22
1.2.1.2	At the Si surface	22
1.2.2	LCP fields of application	24
1.2.2.1	Wafering	24
1.2.2.2	Edge isolation and passivation opening	25
1.2.2.3	Selective doping	25
1.3	This work	27
2	Experimental setup and characterization methods	29
2.1	LCP setup	29
2.2	Characterization methods	32
2.2.1	Imaging	32
2.2.2	Lifetime measurement	33
2.2.2.1	QSSPC measurement	33
2.2.2.2	Rear Surface Recombination Velocity (SRV)	39

Contents

3	Deep grooving	45
3.1	Influence of process parameters on groove depth and continuity . . .	46
3.1.1	First study on dependence of grooving quality on process parameters	47
3.1.2	Interruptions features	51
3.2	Optimizing the 150 μ m-depth grooving	51
3.3	Conclusions	55
4	Doping while shallow grooving	59
4.1	Short qualitative description of H_3PO_4 -grooving induced effects . .	60
4.2	Evaluation of SRV for different LCP paths	61
4.2.1	Selecting parameters on the basis of QSSPC-measured lifetime	61
4.2.2	Applying Fischer/Plagwitz method to evaluate SRV induced by H_3PO_4 -grooving LCP	62
4.3	Results and Conclusions	65
5	Summary	69
	Bibliography	73
	Appendix A: LEE laser optical losses and pulse duration	77
	Appendix B: Deep spots at the groove beginning	79
	Appendix D: Supplement to Chapter 4	83
	Aknowledgments	85

List of Figures

1.1.1 Sketch of a solar cell	14
1.1.2 [3, 11]Dark and illuminated solar cell response	14
1.1.3 [30]Absorption coefficient and absorption length in silicon. Short wavelength photons are absorbed within several tenth of microns, while long wavelength photons ($\lambda \sim 1000nm$) need several internal reflections before being absorbed within cell thickness.	16
1.1.4 Resistance losses	17
1.1.5 [11]PERL high-efficiency monocrystalline silicon cell structure . . .	19
1.2.1 [4]Sketch of the LCP principle	21
1.2.2 [4]Effects occurring at the beginning of the laser pulse, before the onset of melting and evaporation	23
1.2.3 [3]Photolithography and LCP for selective emitter formation	26
1.3.1 Sketch of the BJ-BC solar cell design under development	28
2.1.1 Intensity profile within the liquid jet (standard LCP doping parameters)	30
2.1.2 LCP Coupling unit	31
2.1.3 Machining axis for LCS, by Synova S.A.	32
2.2.1 Confocal microscopy: a schematic	33
2.2.2 Instrument for photoconductance measurement: a schematic	34
2.2.3 [6](Top) The current flow for widely spaced contacts is expected to be independent of the neighbouring points. (Bottom) If the points are closely spaced compared to W , the current flow will be largely parallel	40
2.2.4 Fischer's method: reference probe for passivation	42
2.2.5 Fischer's method: front side probe	43
2.2.6 Fischer's method: reference probe for passivation	43
3.0.1 Examples of interrupted LCP-processed grooves where the interruption is at the beginning (3.0.1a) or all along (3.0.1b) the line length .	45

List of Figures

3.1.1 LEXT image of an interrupted groove cross section, @400bar, 0.7764mJ, 10mm/s . The orange sectioning plane highlights the saw-tooth shape of the interruption cross section	51
3.1.2 SEM and LEXT images showing interruption periodicity	52
3.2.1 Graphs of results from second grooving test	54
3.2.2 LEXT images of grooves obtained with multipass mode	57
4.2.1 Effective lifetimes measured by QSSPC are plotted, on a logarithmic scale, as a function of the pulse energy	62
4.2.2 Sketch of reference and processed samples according to Fischer/Plagwitz scheme	64
4.2.3 An example of a wafer processed by LCP. The four fields are processed each with a different pitch	66
4.2.4 An example of a fit curve of SRV on pitch, given by the Mathematica7.0 script.	66
4.3.1 SRV is plotted in bilogarithmic scale as a function of pulse energy .	68
4.3.2 LEXT image of a doped groove obtained with a LEE laser processed field (@160bar, 0.2768mJ, 100mm/s) where the pitch is $3000\mu m$. .	68
5.0.1 Sketch of a processed wafer with 24 fields	81

List of Tables

2.1.1 LCP parameters definition and values used in this work	31
3.1.1 Range of parameters to study grooves processing with LCP	46
3.1.2 Parameters used for the first grooving test.	47
3.2.1 Parameters used for further grooving test	53
3.2.2 Relevant data for grooves processed with multi-pass mode	55
4.0.1 Parameters for standard doping LCP	59
4.3.1 SRV results from lifetime QSSPC data elaborated by means of a Mathematica7.0 script written at Fraunhofer ISE.	65
5.0.1 LEE absorption and pulse duration data for different pulse repetition rates	77
5.0.2 First parameters used for QSSPC measuring	83

1 Introduction

The frame to this work is the research in photovoltaics and, more in detail, in silicon solar cells. Photovoltaics is a fast growing market, with wafer-based silicon solar cells having the widest market share.

In order to lower production costs with the aim of a large solar cells widespreading, research is performed to introduce new processes for low-cost high-efficiency concepts.

The LaserChemicalProcessing, which potentialities are investigated in this work, is one of the promising laser application for this purpose.

1.1 Silicon Solar Cells

A simplified cell concept for a p -type silicon solar cell is sketched in Fig. 1.1.1. The operation principle can be generalized to any solar cell design.

A thin n -type emitter layer is created on a p -type layer, thus originating a $p - n$ junction. The absorption of the incident light illuminating the front surface generates an electron-hole pair, which has to reach the $p - n$ junction by diffusion in order to be separated by the electric field of the space charge region. The collection probability fastly decreases with increasing distance between the point of generation and the edge of the space charge region. The minority carrier diffusion is then of great importance in determining the probability for generated carriers to be effectively collected. The absorption coefficient for high energetic blue wavelengths is much higher than for shorter wavelengths. The short wavelengths absorption takes place closely to the front surface (tenth of microns) and for this reason, the $p - n$ junction is brought close to the front.

The ideal behaviour of a solar cell is described by the $I - V$ curve:

$$I = I_o(e^{-qV/k_bT} - 1) - I_L \quad (1.1.1)$$

1 Introduction

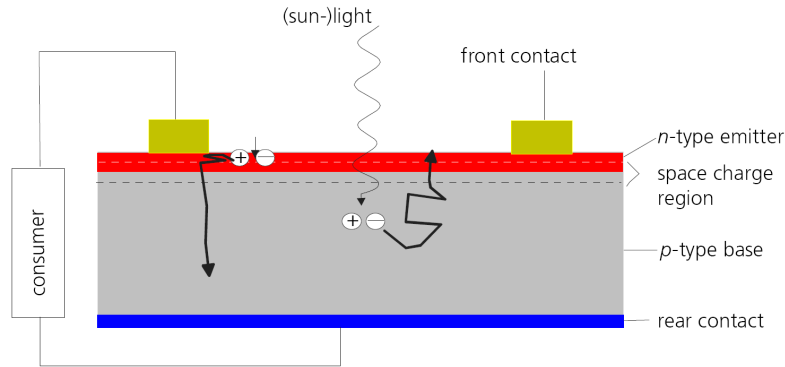


Figure 1.1.1: Sketch of a solar cell

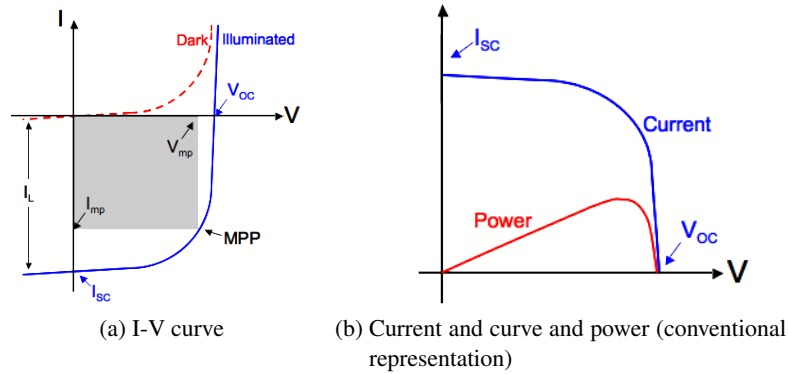
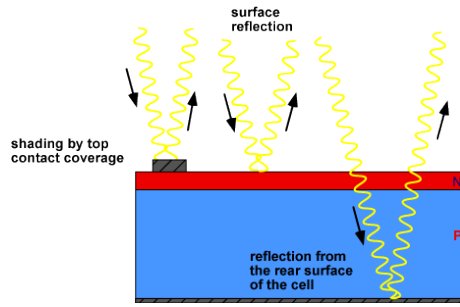


Figure 1.1.2: [3, 11] Dark and illuminated solar cell response

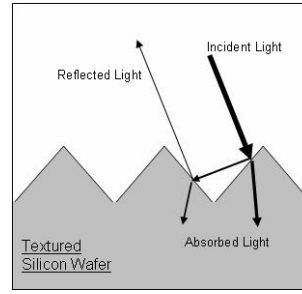
where I_o is the saturation current and I_L the photogenerated current. Note that for $I_L = 0$, that is, in dark the equation is that of a diode (see Fig. 1.1.2)

The short circuit current I_{sc} , the open circuit voltage V_{oc} , the fill factor FF and the efficiency η are the parameters commonly used to characterize the solar cell behaviour. The I_{sc} is the current flowing when front and back contacts are shortcircuited. V_{oc} is the voltage difference between front and back contacts when no current is flowing. Its expression comes from Eq. 1.1.1 where the current has been set to zero:

$$V_{oc} = \frac{k_b T}{q} \ln \left(\frac{I_L}{I_o} + 1 \right) \quad (1.1.2)$$



(a) [3] Sketch of optical losses by shadowing and reflection



(b) [3] Effect of texturization on light absorption probability

The maximum power point MPP is the operating point where the maximum power can be drawn from the cell. The values of I and V at the MPP, indicated by I_{MPP} and V_{MPP} , are used to calculate the fill factor FF :

$$FF = \frac{I_{MPP}V_{MPP}}{I_{sc}V_{oc}} \quad (1.1.3)$$

which graphical representation is the shaded area in Fig. 1.1.2. The efficiency η can be calculated as the ratio of the maximum output power to the incident light power:

$$\eta = \frac{I_{MPP}V_{MPP}}{P_{light}} = \frac{V_{oc}I_{sc}FF}{P_{light}} \quad (1.1.4)$$

1.1.1 Losses

Several sources of losses are responsible for a cell behaviour far from ideality.

1.1.1.1 Optical losses

A first source of optical loss in conventional cells is the metal grid shading. To reduce or eliminate this contribution, solar cells are designed that have contact bus-bars on the back (leaving only contact fingers on the front) or directly the whole metallization paths on the back.

A second important source of loss is due to reflection on the silicon surface. Silicon surface is then textured by means of a pyramid structure in order to enhance the probability for reflected light to be absorbed (see Fig. 1.1.3b). In addition, coverage with antireflection layers is usually applied.

1 Introduction

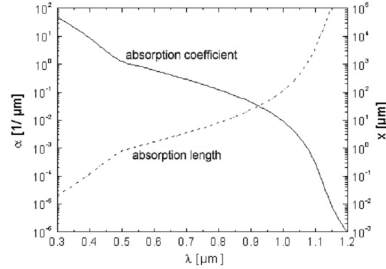


Figure 1.1.3: [30] Absorption coefficient and absorption length in silicon. Short wavelength photons are absorbed within several tenths of microns, while long wavelength photons ($\lambda \sim 1000\text{nm}$) need several internal reflections before being absorbed within cell thickness.

Absorption probability depends on the wavelength. High energy photons encounter a higher absorption coefficient and are absorbed in the first tenth of microns (see Fig.1.1.3). Longer wavelengths ($\lambda \geq 1000\text{nm}$) are weakly absorbed within the wafer thickness and can leave the bulk or be reflected at the rear. Increasing the rear reflectivity is used to enhance the long wavelength response.

1.1.1.2 Recombination losses

Once an electron-hole pair is generated, it is exposed to several recombination mechanisms which occur in parallel. The recombination rate is the sum of those for the individual processes.

Being silicon an indirect gap semiconductor, radiative recombination is negligible.

Auger recombination Auger effect is a three particles process. The energy released by an electron-hole recombination happens to excite another electron or hole, which then relaxes by phonon emission.

The characteristic lifetime associated with the Auger process is depending on the carrier concentration N_D through: $\tau_{Auger} = 1/C_n N_D^2$ (for electrons), where C_n is the Auger recombination constant.

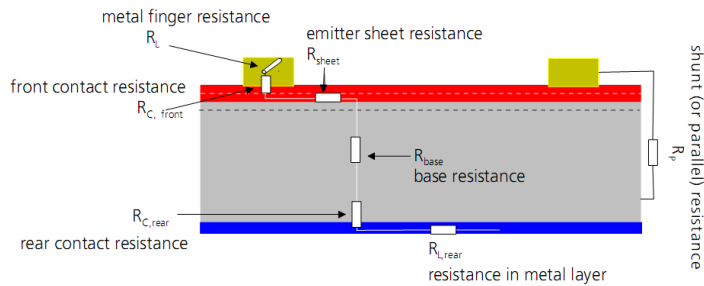


Figure 1.1.4: Resistance losses

Volume recombination: (Shockley-Read-Hall) States within the energy gap due to impurities and defects in the crystal can promote a high efficiency two-step recombination process. The more the states are close to the midgap, the more detrimental the effect. The lifetime defined by Shockley, Read [31] and Hall [31, 10] for this process is a function of the injection level and doping density, as well as traps parameters (concentration, energy level, capture cross section).

Surface recombination Surfaces produce a continuum of allowed states within the forbidden gap. The quantification of surface recombination processes is made via the surface recombination velocity SRV. The two possibilities to reduce surface recombination are:

- reduction of the density of interface states by means of appropriate dielectric layers, such as SiO_2 , that can passivate the dangling bonds
- reduction of the surface carrier concentration, since a reduction of one carrier type can prevent from recombination. This can be achieved by a field effect passivation, where the electric field is generated either by heavy doping the surface (as for example in back surface field, BSF) or by introduction of fixed charges.

1.1.1.3 Resistance and shunt losses

Resistance losses within the cell can lead to power dissipation (see Fig. 1.1.4) and

1 Introduction

should then be minimised by maximising shunt (parallel) resistance and minimising series resistances. The sources of series resistance are:

- contacts: non-zero contact resistance and ohmic losses in the metallization would require large contact areas and broad contact lines. However, this would increase shadowing and recombination
- emitter: in order to have a low emitter series resistance, that enables a good current flow towards the contacts, a highly doped emitter is required. Although, this increases Auger recombination.
- bulk: bulk resistance could be decreased by a higher base doping, which would in turn increase the Auger recombination, or a thinner base substrate, which would however reduce the absorption probability for the longer wavelengths and the mechanical strength.

The shunting between p-type and n-type areas (direct contact of front metallization with the base) should be minimized by maximising the shunt resistance (parallel resistance).

1.1.2 High efficiency concepts

The standard industrial solar cell design is simplified in Fig.1.1.1, where the emitter doping is uniform, the front side has a screen-printed metallization grid and the backside is metallized and passivated by Al-BSF (BackSurfaceField). Due to the limitations introduced by the design itself and the industrial technologies that are used, this kind of solar cell cannot reach high-efficiency. For example, screen printing gives wide fingers on the front side, that is, high shadowing; moreover, Al-BSF is not the best solution in terms of recombination and mirror properties. Finally, the uniform emitter comes from a compromise between blue-response increasing and contact resistance lowering, as explained before.

High efficiency is achieved substantially by minimising losses. The important concept of the selective emitter is introduced, which consists of a n^+ -emitter optimized for blue sensitivity with local n^{++} heavy doping underneath the front contacts. This reduces the contact resistance at the metal-semiconductor interface without decreasing the blue response and allows for narrower contacts as well (the lower the contact resistance, the less the finger width).

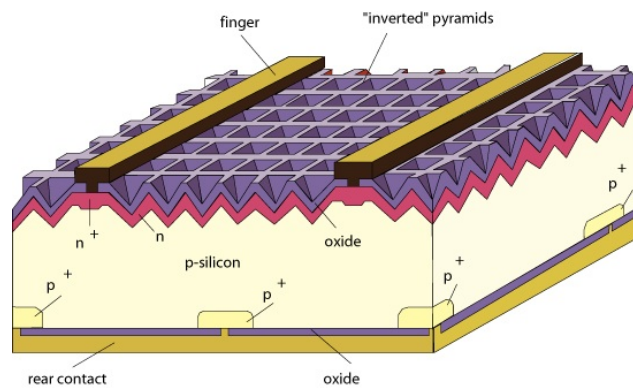


Figure 1.1.5: [11]PERL high-efficiency monocrystalline silicon cell structure

Two examples of high efficiency designs are PERL (passivated emitter, rear locally diffused) and BC (Back-Contact).

1.1.2.1 PERL (Passivated Emitter Rear Locally diffused)

The PERL design for monocrystalline silicon solar cells is sketched in Fig. . The double antireflection layer, together with the photolithographically inverted-pyramids texture reduces the optical losses at the front surface. Moreover, an aluminum evaporated mirror enhances the long wavelength absorption via light trapping.

Both sides are passivated with silicon oxide to avoid surface recombination.

The bulk is thick in order to increase absorption probability in the IR, and the necessary high carrier lifetime is ensured by the high-quality crystalline bulk material.

Finally, contact resistance and recombination at the contacts is minimised by local doping. A $n^+ - n^{++}$ selective emitter is formed at the front surface, and a boron diffused p^+ at back side .

1.1.2.2 Back Contact solar cells

Bringing the metal contacts on the back side has the big advantage to significantly reduce shadowing. Three structures for back contact design are described in the following¹.

¹See [?]

1 Introduction

Metallization Wrap Through (MWT) In these cells, the emitter is located near the front surface, but part of the front metallization grid is moved to the back surface, typically, the broad busbars. The remaining front surface grid is connected to the pads on the rear by means of spot-like openings that go through the wafer.

Emitter Wrap Through (EWT) Here the front surface has no metallization. The emitter is still located near the front surface but the whole metallization grid is moved to the rear. The electrical contact between the front emitter and its contacts on the rear is provided by extending the emitter in the walls of holes through the substrate. On the rear side, the emitter and the base grids are interdigitated.

Back Junction (BJ)² In Back-Junction, Back-Contact solar cells design, also the emitter is moved to the back side.

1.2 Laser Chemical Processing (LCP)

Laser Chemical Processing is based on the LaserMicroJet technology, developed by Synova S.A., that exploits a thin waterjet as a waveguide for a laser beam. The jet is built by pumping water through a sharp edged nozzle with pressure on the order of hundreds bar. A glass window on the nozzle allows a laser beam to be coupled into the jet and to be waveguided to the target surface. The laser induce melting and evaporation on the target and the jet carries away the ablated material. LaserMicroJet is mainly used for cutting of different materials.

In 2003 at the Fraunhofer Institute for Solar Energy systems (ISE), which is now the only institution developing LCP application for silicon solar cells, Willeke and Kray [?],[22] introduced LCP by replacing water with a solvent containing suitable chemicals. The variety of thermal, fluid dynamic and chemical effects thus enabled at the reaction spots can be exploited in different ways. Some examples are microstructuring, e.g. opening of passivation layers or edge isolation, wafering, local doping, aimed at selective emitter and local back surface field (LBSF) formation, and local metallization.

In the following paragraphs the main physical effects involved in LCP will be described, together with some examples of application and latest results.

²On the same topic, see also [8, 18, 7]

1.2 Laser Chemical Processing (LCP)

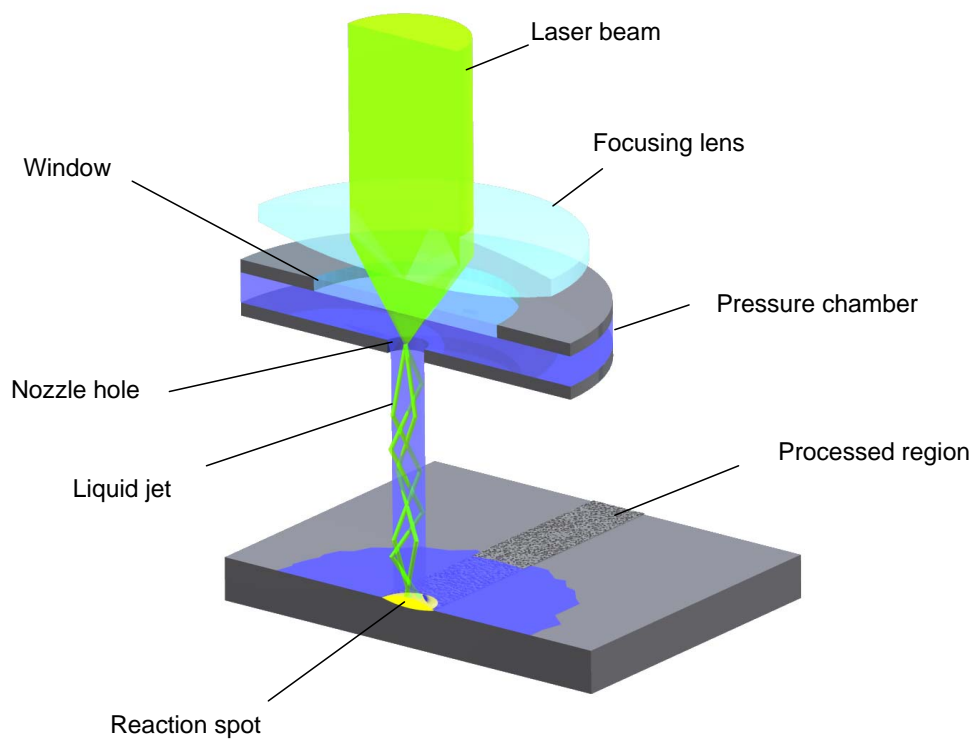


Figure 1.2.1: [4]Sketch of the LCP principle

1 Introduction

1.2.1 Physical effects in LCP

This section is mainly based on the PhD thesis by Andreas Fell, which deals with LCP physical modeling and a new simulation tool development . At the state of the art no other LCP specific literature is available.

The wide variety of physical effect taking place during LCP, and by the way the strong coupling between them, makes an analytical treatment very complicated. Since the aim of this section is simply to introduce the reader to LCP, the following description will be kept on a qualitative way, though having a rigorous background³.

1.2.1.1 From nozzle exit plane to the target surface

The nozzle leads the pumped liquid into a thin jet by means of an aperture of diameter ranging from 50 to 100 μm . The sharp nozzle edge causes the jet to be confined to diameter that equals the 83% of the nozzle aperture[14] and induce laminar flow, which is a fundamental feature if waveguiding is wanted.

A laser beam is focused through a glass window on the nozzle opening plane. The fact of being the refraction index of water higher than surrounding air makes the jet able to confine the laser light via total internal reflection, thus constituting a multimode waveguide. The interference of the different beam modes generates a non uniform intensity distribution on the cross section, where intensity peaks depend on nozzle diameter and coupling optics[1].

With a suitable chemical solution as a liquid medium, photochemical reactions can be induced already in the jet. This is not the case of experiments in this work, since the applied wavelength of 532nm is not absorbed in the liquid jet⁴.

1.2.1.2 At the Si surface

According to optics laws, the laser light is partially reflected by the silicon surface and partially absorbed. The energy thus converted to a thermal form through absorption is responsible for the thermodynamics effects that take place in the silicon target.

³For a rigorous approach, see [4]

⁴In the LCP research group also a 1064nm Nd:YAG is commonly used. This wavelength is absorbed by water. Moreover, IR absorption by suitable chlorine solutions is used to generate radicals.[15, 17]

1.2 Laser Chemical Processing (LCP)

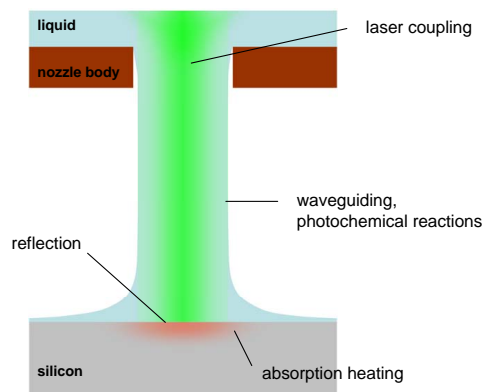


Figure 1.2.2: [4]Effects occurring at the beginning of the laser pulse, before the onset of melting and evaporation

Under the heating effect, once the melting temperature is reached, silicon undergoes a phase change to liquid, which can be described with an enthalpy based approach. The reached high temperatures can also promote thermo-chemical reactions if a liquid else than water is used. In our case, where a H_3PO_4 solution is used as liquid jet, thermal activated phosphor atomization allows phosphor to diffuse into the molten silicon⁵.

The heat transport in silicon is such as to give slow melt cooling kinetics, thus resulting in molten sylicon to solidify in a crystalline rather than amorphous form.

If the absorbed energy is sufficient, silicon can undergo also a second phase transition from liquid to vapour. Here an enthalpy based approach is not applicable if high laser intensities are involved, since the significant superheating requires a different model. Fast evaporation produces a dense vapour plume, which exerts a recoil pressure to the melt⁶, and for high powers even a plasma phase, which can act as an optical shield.

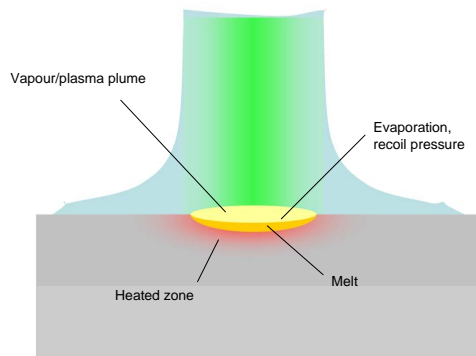
The fluid dynamics effects involving liquid jet impinging on the surface, silicon melt and, if applicable, silicon vapour are influenced by the kinetics of heating and cooling through the so called “melt duration”. To simplify, as long as the silicon is liquid, it can be moved, and thus ablated, by the high pressure liquid jet.

It is important to underline that not only the physical effects themselves are to be

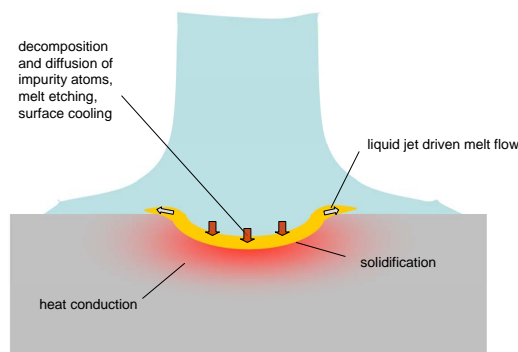
⁵Phosphor diffusion coefficient in liquid silicon is several orders of magnitude higher than in solid, thus allowing a fast diffusion kinetics.

⁶Recoil pressure can reach high values for short pulses, namely, $1GPa$. It is exerted only during the evaporation

1 Introduction



(a) Effects during the laser pulse after the onset of evaporation



(b) Effects after the laser pulse

considered, but also their kinetics, being the relative time scale of great importance in defining the degree of interaction between the phenomena.

1.2.2 LCP fields of application

1.2.2.1 Wafering

The usual process to cut wafers out of a crystalline silicon ingot is multi wire slurry saw (MSWT). A thousand of parallel wires can abrasively cut wafers with a thickness down to $150\mu m$, heaving a kerf loss of at least the same amount. The wafer surface results damaged and contaminated, especially by metals from the wire, and has to undergo wet chemical etching and cleaning steps, which increase the overall loss of silicon.

1.2 Laser Chemical Processing (LCP)

LCP could be a suitable alternative to MSWT, even if wafering by LCP is still in the stage of fundamental research. The ability of 7cm cutting depth has been proven [21, 16, 5] and the ongoing research is focusing on investigating laser parameters and chemical additives. Recently, Mayer [24] proved the good influence on cut quality by addition of chlorine. The big advantage in regard to to the MSWT, is to reduce the silicon losses by means of smaller kerfs and a better surface quality, which makes additional etching and cleaning unnecessary.

1.2.2.2 Edge isolation and passivation opening

In order to form the electrical contacts or, in high efficiency cell designs, to form a selective emitter by diffusion, the passivation layer on the silicon surface has to be opened.

LCP with water as a liquid medium can be applied instead of the usually techniques, namely, photolithography or dry laser processing, without requiring mask preparation or damage removal.

1.2.2.3 Selective doping

As discussed in the previous section, high-efficiency solar cells design requires a lowly doped emitter with a high blue response. Directly under the metal contacts, however, a high surface doping minimises contact resistance and recombination. This is the idea of selective emitter. Usually, selective emitters are produced by photolithography, which is not suitable for an industrial application, due to the several time-consuming and cost-intensive masking and etching steps.

With LCP local high doping can be achieved in a fast single step. Phosphor is used for n-type doping, with phosphoric acid is as a liquid medium. A short comparison of the photolithography and Lcp in terms of process steps is given in Fig.1.2.3. Solar cell results with LCP doping have been published in [20], where LCP with low nanosecond pulse laser is shown to produce a proper selective emitter.

In addition to the selective emitter formation, local doping can also be applied to create a local back surface field (LBSF). Similarly to the case of the front surface, if the back surface is contacted only locally, a highly doped layer reduces recombination. For p-type solar cells, p-type doping is required for the BSF. With LCP using

1 Introduction

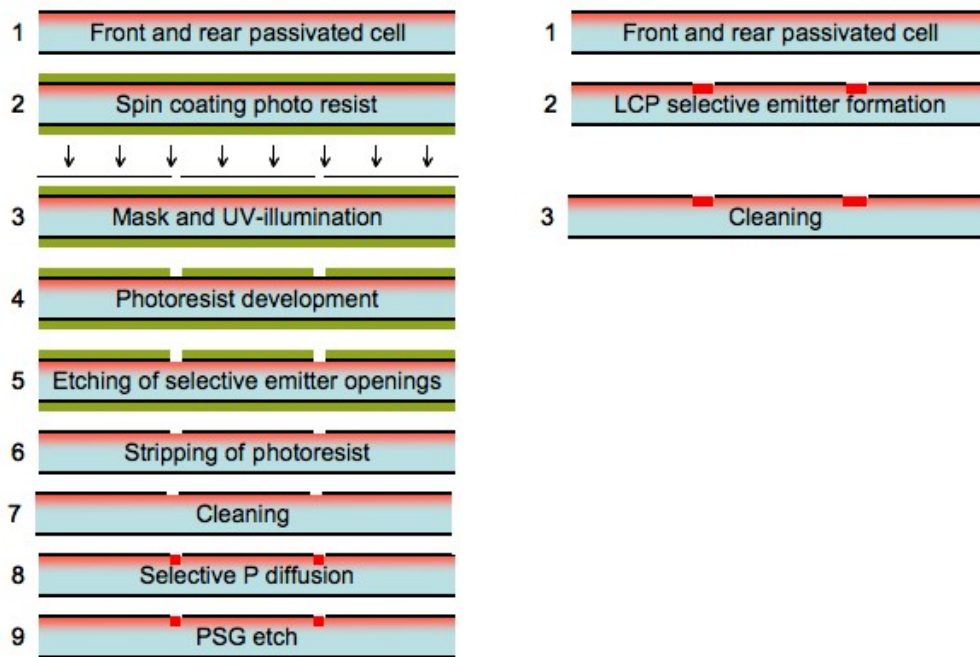


Figure 1.2.3: [3]Photolithography and LCP for selective emitter formation

a boron-containing liquid, fast local p-doping with passivation layer opening can be achieved in a single step.[19]

1.3 This work

This thesis summarizes the experimental work carried out by the author during a nine months collaboration with the MLV group, led by Filip Granek, of the Fraunhofer Institute for Solar Energy systems (ISE) in Freiburg, Germany.

The main goal of this work is to investigate the possibility of LCP for grooving and doping in one step. The interesting potential of LCP technology arises from its being much easier and cost-effective compared to the alternative technologies. The state-of-the-art technologies to get doped grooves are based on dry laser or photolithography. Dry laser grooving has to be followed by damage etching, followed by a (masked) dopant diffusion step. Photolithography is an expensive, time-consuming technology since it requires several process steps, based on different mask designs.

Up to now, doping with LCP was performed just by processing the surface. The question about the feasibility of simultaneous structuring and doping is not answered yet, though previous first results with higher energy density were not promising [16]

This work focuses on two main topics: on one side the morphology of the deep structures will be studied in a wide range of parameters for water-processed grooves. On the other side, the effective result of damage and doping damage induced at the rear side, in terms of surface recombination velocity, will be studied for shallow, H_3PO_4 -processed grooves⁷

In the context of Back Junction, Back Contact(BJ-BC) solar cells, a new high efficiency cell design is being developed at Fraunhofer ISE. Its main features are, as sketched in Fig. 1.3.1 a) a p -type doped monocrystalline base, b) a front diffused n^+ -doped layer, which acts as a front passivation, c) p^{++} BSF, d) interdigitated contacts and d) n^{++} -emitter all around an array of e) deep ($\simeq 150 \mu\text{m}$ on $200 \mu\text{m}$ -thick wafers) grooves, which aim is to bring the $p - n$ junction as closer as possible to the front surface, in order to reduce the path for minority carriers to be collected.

This design requires then to open deep grooves in the silicon substrate, and to selectively dope their surface. LCP could be a promising, cost-effective solution, either in

⁷In this work, “deep” means $\sim 100 - 200 \mu\text{m}$, while “shallow” refers to the tenth of μm order.

1 Introduction

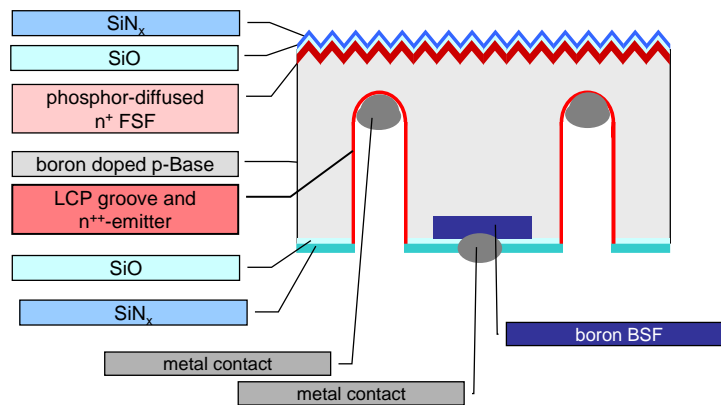


Figure 1.3.1: Sketch of the BJ-BC solar cell design under development

the case that selective doping is achieved by a separate diffusion step after the LCP-grooving (which implies the use of a water jet for LCP), or that both grooving and doping are made by means of LCP (here with a dopant-medium jet, namely, H_3PO_4).

Another area of application for deep 3-D structures obtained with LCP could be the MWT (Metal-Wrap-Through) or the EWT (Emitter-Wrap-Through) designs [?] (see par.1.2), as well as the Buried Contact solar cell manufacturing [35].

From the previous examples, it is now evident that a good understanding of structuring and doping potentiality of LCP, either with water or phosphoric acid, is of great interest.

2 Experimental setup and characterization methods

2.1 LCP setup

LCP is performed by means of three main parts: a laser system, a pump and a coupling machine.

Pump Two different pumps were used in this work. The one (Wandfluh) can produce an output waterjet pressure ranging from 50 bar to 500 bar, while the other one (Besta) can pump either water or H_3PO_4 up to a pressure of about 180 bar.

Laser systems Two different laser systems are used here for LCP, which characteristics are listed in the chart below.

	Type		λ [nm]		Power _{max} [W]	Mode	Pulse duration [ns]
LEE	Nd:Yag	diode pumped	532	2nd harmonic	59.93	Q-sw	$\sim 108 \div 480$
HIPPO	Nd:YVO ₄	diode pumped	532	2nd harmonic	6	Q-sw	~ 10

In this work, a Q-switched, 532 nm laser beam has been used, produced by doubling the main output frequency from either the *Nd : YAG* (LEE) laser or the *Nd : YVO₄* (HIPPO) laser. The second harmonic wavelength of 532nm has been preferred to the main output wavelength of 1064nm because of the strong absorption of IR light in water .

The laser beam is carried to the coupling machine by means of an optical fiber. This, together with other optical coupling losses, induces the laser light power to be attenuated . Measured values of laser power before (*internalLpow*) and after (*Lpow*) the

2 Experimental setup and characterization methods

fiber reveal an average fiber attenuation factor of about 30%. (See5). If not differently specified, the energy density values in the following work are calculated on the basis of measured external laser power, that means at the fiber exit plane.

Another effect that has to be mentioned is that the intensity profile in the cross section of the liquid jet is not homogeneous, presenting peaks due to the interference of the different modes propagating [4], as can be seen in Fig. 2.1.1 .

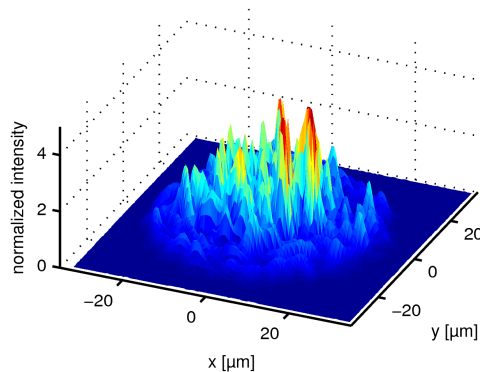


Figure 2.1.1: Intensity profile within the liquid jet (standard LCP doping parameters)

Coupling machine The coupling machine has two main tasks: to carry out the coupling of the liquid jet and the laser beam, which has previously been elaborated and focused by an optical head, and to provide an axis system for movement of the sample.

The effective matching of the input jet and laser beam is carried out by an especially designed coupling unit, which consisting parts are highlighted in Fig.2.1.2 . The heart of the coupling unit is a nozzle, typically made of brass with a sapphire nozzle stone, which is shaped to allow the outcoming liquid jet to be laminar; a glass window lets the laser beam out, directly into the laminar jet, as shown in Fig. . Different nozzle diameters are available, ranging from 50μm to 150μm.

A Helium flux around the jet improves the laminarity of the jet itself.

The two coupling machines used during this work are named LCS and R&D, by the company Synova S.A.. In the former, the sample is placed on a chuck that can move on one axis, while the optical head moves in the other two axis (see Fig.2.1.3). In

2.1 LCP setup

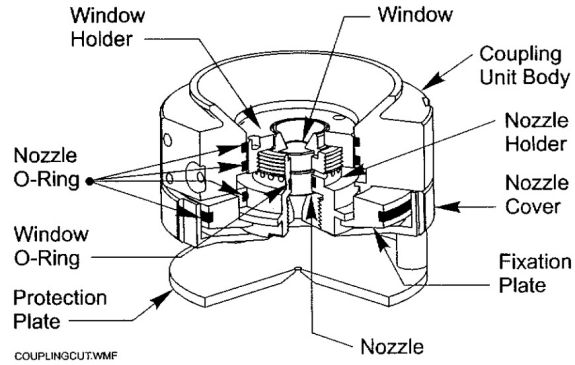


Figure 2.1.2: LCP Coupling unit

the latter, the chuck can move in the two axis on its plane, while the optical head is fixed (See Fig.2.1.3). In both cases, the processing is controlled by suitable CNC programmes.

The samples used for this work have been processed with three main setups: a) R&D machine, Besta pump with LEE or b) HIPPO laser and c) LCS machine, Besta or Wandfluh pump with LEE laser.

The main parameters characterizing the LCP processing can be summarized in Tab. 2.1.1, where the values assumed are the ones relevant for this work:

Variable		Unit	Controlled by	Range of values	
$Press$	jet pressure	bar	pump	[50; 400]	Wandfluh
				[50; 180]	Besta
L_{pow}	laser power	W	laser system	[0; 60.3]	LEE
				[0; 6]	HIPPO
$Freq$	pulse repetition rate	kHz	laser system	{15; 50}	LEE
				{35} ¹	HIPPO
E_p	pulse energy	mJ	laser system	calculated as $E_p = L_{pow}/Freq$	
$\Delta\tau_p$	pulse duration	ns	laser system	$\sim 1 \div 10$	HIPPO
				$\sim 100 \div 500$	LEE
Ssp	scanning speed	mm/s	coupling machine	{2; 100}	

Table 2.1.1: LCP parameters definition and values used in this work

2 Experimental setup and characterization methods

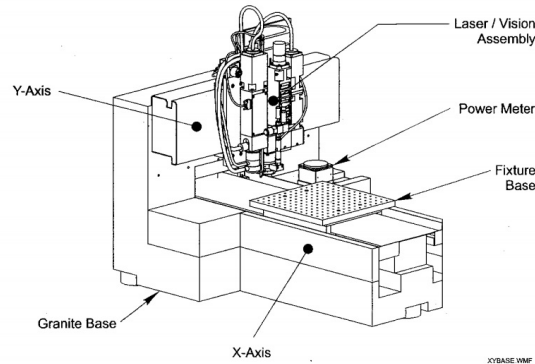


Figure 2.1.3: Machining axis for LCS, by Synova S.A.

2.2 Characterization methods

2.2.1 Imaging

At various stages in this work, the imaging techniques have turned out to be very useful, especially in analyzing the grooves quality in terms of cross-section regularity and surface roughness. Mainly, two instruments have been used: a SEM (Scanning Electron Microscope) and an optical 3D measuring laser microscope (Olympus-LEXT). In addition to confocal and electron beam microscopes, also an optical microscope has been used.

Lext The LEXT microscope exploits the combination of a confocal and a white light microscope, being the illumination source either a laser beam (405nm) or a LED-white light. The use of the laser illumination allows to get 3D images in high spatial resolution (namely, 7nm in z-direction and 120nm on the x-y plane) by overlapping the “slices” obtained by scanning the x-y plane at different z coordinate, as sketched in Fig2.2.1. At each z-position, only the light reflected by the plane of focus is collected and converted to a digital form, to be elaborated by a computer.(**)

Scanning Electron Microscope In Scanning Electron Microscope a thermo-ionically emitted electron beam is used to scan the sample surface. One of the different effects induced in the sample is then detected, namely, backscattered electrons generated by

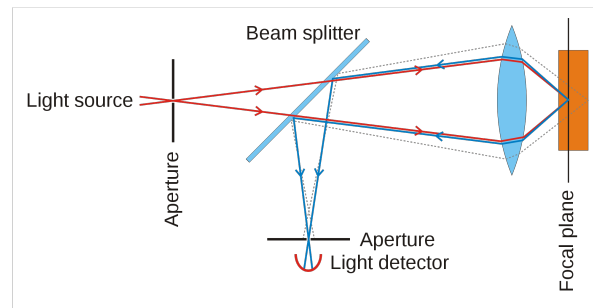


Figure 2.2.1: Confocal microscopy: a schematic

elastic scattering, secondary electrons emission by inelastic scattering, cathodoluminescence and induced current by electron-pairs generation in semiconductors, and X-rays generation. SEM images in this work have been taken by secondary electron imaging.

2.2.2 Lifetime measurement

In order to assess the impact of doping with Laser Chemical Processing, lifetime reduction in the silicon wafer after LCP has been chosen as the most relevant parameter, the value for lifetime τ being obtained from Quasi-Steady-State Photoconductance (QSSPC) measurement. QSSPC finds also an interesting application in the determination of the surface recombination velocity for rear contacted solar cells, proposed by Fischer [6] and Plagwitz [26], which allows, e.g., to deeper investigate the damage induced by LCP.

2.2.2.1 QSSPC measurement

Lifetime test structures are designed to let the effect of interest dominate. If the volume lifetime has to be studied, then the surface recombination is kept as low as possible; if surface has to be studied, then high-lifetime bulk material will be used. In general, both the recombination in volume and at the surface contribute to determine the effective lifetime that is determined by the measurement, τ_{eff} .

The idea on the basis of photoconductance measurement is to evaluate the excess carrier lifetime by monitoring the decay of excess carriers that have been photogenerated

2 Experimental setup and characterization methods

by a pulse-like flash of white light.

The relationship between excess carrier lifetime τ_{eff} , average excess carrier density² Δn_{av} and measured photoconductance σ_L will be given more explicitly in the following paragraphs.

The photoconductance instrument, the Sinton WCT-120 by Sinton Consulting Inc., is sketched in Fig. 2.2.2. A coil, located in close distance under the sample, is part of a circuit which provides a nearly linear conductance to voltage conversion. The electromagnetic field in the vicinity of the coil couples to free carriers in the sample and causes eddy currents. These induce an opposite current in the coil but they are also subject to resistive losses in the sample and screen the magnetic field in layers more remote from the coil [19].

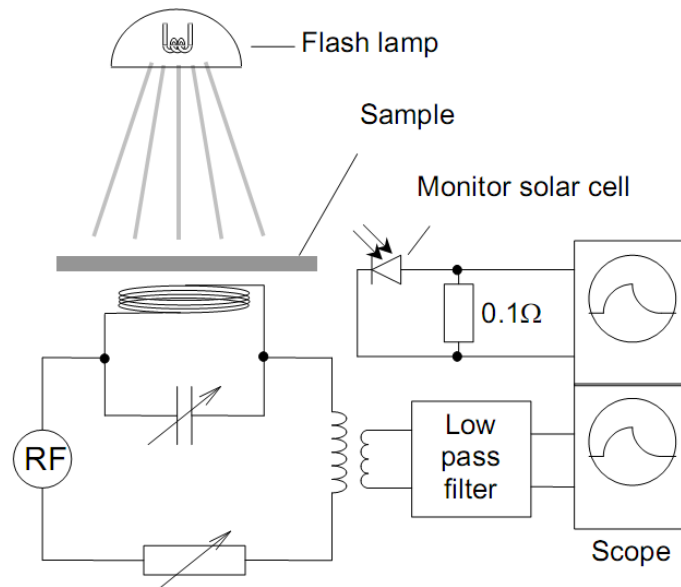


Figure 2.2.2: Instrument for photoconductance measurement: a schematic

The photo-flash has a spectrum similar to that of the sun and a pulse-like intensity

²In general, the excess carrier density is position dependent. The average density Δn_{av} used in the following equations is given by the the total number of carriers divided by the wafer thickness. However, as shown later on, the effective lifetime determined from a photoconductance measurement does not depend on the details of the minority carrier distribution, except for a very weak dependence introduced by the carrier mobility evaluated at average carrier concentration.

profile chosen to be described by a steep turn-on ramp, a short plateau and an exponential decay [25]. By setting the pulse duration, different measurement modes are allowed. If the flash time constant is much longer (in the milliseconds range) than the lifetime in the sample (usually in tenth to hundreds μs range), the excess carrier distribution is essentially in steady-state and then a steady-state photoconductance is measured. On the opposite case, when the flash decay time is set to be much shorter than the lifetime in the sample, the photoconductance decay transient is observed.

Since the transient approach requires a light pulse with very steep cut-off ramp and fast electronics for recording the photoconductance decay [25], an alternative carrier lifetime method based on quasi-steady state illumination has been proposed by Sinton *et al.* [33, 32]. The quasi-steady-state condition is applicable when the flash decay constant is comparable with the effective lifetime in the sample.

All the lifetime measurements in this work used the quasi-steady-state photoconductance (QSSPC) technique.

Spatially uniform photogeneration and zero surface recombination

In order to describe the effects induced by photogeneration, the simplest case of spatial uniformity and zero surface recombination is firstly analyzed. Here the photogeneration $G(z, t)$ and the recombination $U(z, t)$ rates are given their average values over the wafer thickness W , as well as the excess carrier density $\Delta n(z, t)$, that can be calculated from the photoconductance. Namely,

$$G(z, t) = G_{av}(t) = \int_{-W/2}^{W/2} G(z, t) dz,$$

$$U(z, t) = U_{av}(t) = \int_{-W/2}^{W/2} U(z, t) dz \text{ and}$$

$$\Delta n(z, t) = \Delta n_{av}(t) = \int_{-W/2}^{W/2} \Delta n(z, t) dz.$$

The effective lifetime is evaluated from³

$$\tau_{eff} = \frac{\Delta n_{av}}{G_{av} - d\Delta n/dt} \quad (2.2.1)$$

This comes from the general continuity equation for the excess electron density

$$\frac{\partial \Delta n(z, t)}{\partial t} = G(z, t) - U(z, t) + \frac{1}{q} \nabla J \quad (2.2.2)$$

³Note the explicit dependence of lifetime on excess carrier density

2 Experimental setup and characterization methods

where the spatial uniformity and zero surface recombination lead to no electric field within the sample. Thus, the last term on the right-hand side of eq. 2.2.2 vanishes and the carrier concentration is spatially uniform

$$\frac{d\Delta n(t)}{dt} = G(t) - U(t) = G(t) - \frac{\Delta n}{\tau_{eff}} \quad (2.2.3)$$

where the classic relationship $U = \Delta n/\tau_{bulk}$ between the recombination rate and the bulk lifetime has been used.⁴

The two extreme cases are a) the steady-state condition, where $\frac{d\Delta n(t)}{dt} = 0$, thus leading to $G(t) = U(t)$, and b) the transient case, that applies for very short flash lamps and thus translates into the condition $G(t) = 0$. The effective lifetimes under steady-state and transient conditions are then, respectively⁵ [25]:

$$\tau_{eff,ss}(\Delta n) = \frac{\Delta n}{G} \quad (2.2.4)$$

$$\tau_{eff,tr}(\Delta n) = -\frac{\Delta n}{d\Delta n/dt} \quad (2.2.5)$$

From the eqs.2.2.1, 2.2.4 and 2.2.5 it is evident that, in order to estimate the effective lifetime τ_{eff} , the knowledge of $\Delta n(t)$ is required.

Relationship between excess carrier density Δn and photoconductance σ_L

It is assumed that the instrument measures the sheet conductance over the depth z of the sample: $\sigma = q \int_0^W (n\mu_n + p\mu_p) dz$.

Provided that illumination creates coupled excess carriers ($\Delta n = \Delta p$) and changes the carrier mobilities to values μ_n, μ_p different from the equilibrium ones μ_{n0}, μ_{p0} , the photoconductance is given by

$$\sigma_L = \sigma_{light} - \sigma_{dark} = q \int_0^W \Delta n(\mu_n + \mu_p) + n_0(\mu_n - \mu_{n0}) + p_0(\mu_p - \mu_{p0}) dz \quad (2.2.6)$$

that, under the hypothesis of spatially homogeneity, reads

⁴Under the hypothesis of no surface recombination that we are considering, $\tau_{eff} = \tau_{bulk}$. See also 2.2.2.1

⁵Note the explicit dependence of lifetime on excess carrier density

$$\sigma_L = qW(\Delta n_{av}(\mu_n + \mu_p) + N(\mu_n - \mu_{n0})) \quad (2.2.7)$$

where an n -type wafer has been considered, so that p_o could be neglected and $n_0 = N$.

Note that, in order to translate the photoconductance value into a lifetime via an average excess carrier density, the knowledge of the sample thickness, doping concentration and charge carrier mobilities is required. Moreover, the evaluation of QSSPC measurement also requires knowledge of the photogeneration rate, which depends on the optical properties of the sample and the spectral distribution of the light source.

As shown by Sinton [33], the photogeneration rate (as well as the recombination rate) can be conveniently expressed in terms of photogenerated current density as: $J_{gen} = q \int_0^W G(z, t) dz = qWG_{av}$.

Under steady-state condition, the 2.2.4 becomes, in terms of J_{gen} ,

$$J_{gen} = \Delta n_{av} qW / \tau_{eff} \quad (2.2.8)$$

and in the 2.2.7 the carrier mobility reaches its equilibrium value μ_{n0} , thus leading to

$$\sigma_L = qW \Delta n_{av} (\mu_n + \mu_p) \quad (2.2.9)$$

The effective minority carrier lifetime can be then determined from Eqs. 2.2.9 and 2.2.8, giving

$$\tau_{eff} = \frac{\sigma_L}{J_{gen}(\mu_n + \mu_p)}$$

In quasi-stady-state condition, it is assumed that the generation rate is written as the sum of the steady state generation rate $G_{av,SS}$ and a term that expresses the time-dependence, thus translating into a photogenerated current:

$$J_{gen,tot} = J_{gen,SS} + J_{gen,tr} = Wq(G_{av,SS} - \partial \Delta n_{av}(t) / \partial t) \quad (2.2.10)$$

Beyond the zero-surface-recombination approximation

2 Experimental setup and characterization methods

In the more general case of nonzero surface recombination, the effective lifetime has to take into account the surface recombination contribution; therefore,

$$\frac{1}{\tau_{eff}} = \frac{1}{\tau_{vol}} + \frac{1}{\tau_S}$$

with

$$\frac{1}{\tau_S} = \frac{\Delta n(W) S_r}{\Delta n_{av} W} + \frac{\Delta n(0) S_f}{\Delta n_{av} W} \quad (2.2.11)$$

where S_r and S_f are the surface recombination velocities on the front and back surface, respectively. The 2.2.11 comes from the time-dependent transport equation for the excess carriers

$$\frac{\partial \Delta n(z,t)}{\partial t} = D_a \frac{\partial^2 \Delta n(z,t)}{\partial z^2} - \frac{\Delta n(z,t)}{\tau_{vol}} + G(z,t) \quad (2.2.12)$$

integrated over the wafer thickness W and where the boundary conditions for the currents disappearing in the front and rear surfaces have been applied[25]. D_a is the ambipolar diffusion constant.

The effective lifetime τ_{eff} is not uniquely defined, since in 2.2.11 the ratio of carrier densities at the surfaces to the average concentration depends on $G(z,t)$. The lifetime expressions for the two extreme cases, i.e. transient measurement and steady state measurement, are given below, where the approximation $S_f = S_r = S$ has been made⁶.

- In transient measurement, $\tau_{S,tr} \approx \frac{W}{2S} + \frac{W^2}{\pi^2 D_a}$. For very low S , $\tau_{S,tr} \approx W/2S$, while for very high S , $\tau_{S,tr} \approx \tau_0/\pi^2$, where $\tau_0 = W^2/D_a$ is the transit time⁷.
- In steady-state measurement, for τ_{vol} large and S small, $\tau_S \approx W/2S$, while for very large S , $\tau_S \approx \tau_0/12$.

To conclude this paragraph, it is worth to note that, since $\frac{1}{\tau_{eff}} = \frac{1}{\tau_{vol}} + \frac{1}{\tau_S}$, the evaluated lifetime τ_{eff} will equal the volume lifetime τ_{vol} for samples with perfect surface passivation. Non-ideal surface passivation, instead, poses an upper limit to τ_{eff} , which is the surface lifetime τ_S .

⁶For the extensive calculations that lead to the following results, see ***

⁷The transit time is the time required for a carrier to traverse the wafer thickness by diffusion

2.2.2.2 Rear Surface Recombination Velocity (SRV)

As shown in the previous paragraph at page 38, if the surface recombination velocity (from now on indicated as SRV) is sought, the 3-dimensional charge transport problem in the sample has to be solved.

Recently, Fischer described an analytical technique to calculate the effective rear SRV of a point contacted solar cell, which has been used by Plagwitz to implement a measurement technique based on lifetime measurement⁸ [26].

Fischer's approach

The approach proposed by Fischer is aimed to reduce to 1D the 3D problem of carrier transport in a rear point contacted solar cell, where the front surface is passivated (thus allowing front SRV to be neglected) and the rear surface passivation is opened where point-like contacts are. The extension to the stripe-like contacts has been added by Plagwitz [26](see 62).

The rear surface is seen as the sum of two parts:

- the contacted surface, described by its fraction f over the total surface and its SRV S_{met} , which contributes to the effective SRV by S_{cont}
- the passivated surface, described by its fraction $1 - f$, complementary to the contacted one, and its SRV S_{pass}

and the effective rear SRV $S_{eff, rear}$ is obtained from the two separate contributions of S_{cont} and S_{pass} . The $S_{eff, rear}$ may then be used in a one-dimensional calculation to include volume recombination.

For a planar geometry⁹ where the transport in the emitter is neglected¹⁰, a simple expression for S_{eff} is calculated

$$S_{eff} = D \left(\sigma R_s - W + \frac{D}{f S_{met}} \right)^{-1} \quad (2.2.13)$$

where D is the minority carrier diffusion constant, R_s and σ the series resistance and conductivity, respectively, in the base and W the cell thickness. With the Eq. 2.2.13, the problem is reduced to finding R_s .

⁸See also [29]

⁹The limits of this assumption will be considered while applying Fischer's model to our case. See 4.2.2

¹⁰The emitter effects can be included in a later stage

2 Experimental setup and characterization methods

The series resistance R_s in a base with a periodic pattern of point-like or line-like contacts on the rear side cannot be calculated analytically; however, Fischer and Plagwitz have described R_s with approximated functions, based on the spreading resistance R_{spread} . R_{spread} is the resistance through a single disk-shaped contact on one side and a full area contact on the other side of an infinitely extended slab. Its analytical expression has two asymptotes for the two limit case of very thin and very thick substrate.

R_s inherits these asymptotical behaviours, which apply to the two cases of very large and very small ratios of pitch (=spatial period) L_p over the substrate thickness W . As shown in Fig.2.2.3, for contact points in very large spacing, i.e., $L_p/W \gg 1$, the contacts are expected not to 'interfere', so that an area of the pitch can be attributed to each contact to give the series resistance $R_s = R_{spread}L_p^2$. On the opposite case, i.e. $L_p/W \ll 1$, with decreasing the pitch, the current will flow more and more parallel, until the resistance is eventually determined by the Ohm's law: $R_s = \rho W$. The final

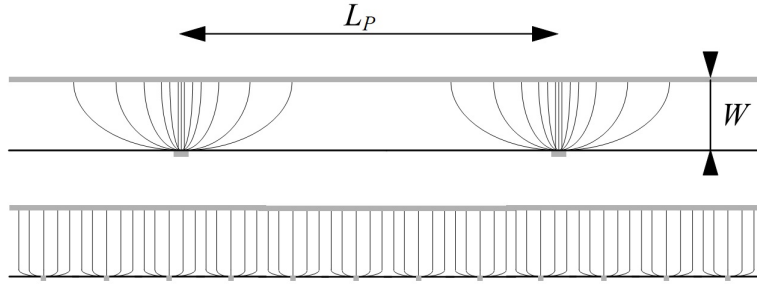


Figure 2.2.3: [6](Top) The current flow for widely spaced contacts is expected to be independent of the neighbouring points. (Bottom) If the points are closely spaced compared to W , the current flow will be largely parallel

general expression for R_s for stripe-like contacts of length l reads then

$$R_s = R_{spread}L_p l + \rho W \left(1 - \exp\left(-\frac{W}{L_p}\right) \right) \quad (2.2.14)$$

where the small pitch contribution is weighted by an exponential in order to vanish as L_p increases.

The effective rear SRV is then calculated by adding the two SRV contributions S_{cont} and S_{pass} , which gives $S_{eff,rear} = S_{cont} + (1 - f)S_{pass}$ for the small L_p limit and $S_{eff,rear} = S_{cont} + S_{pass}/(1 - f)$ for the large L_p limit .

Measuring SRV after rear side LCP as an application of Fischer's approach

Fischer's approach can be applied also to non-contacted, rear LCP-processed Si substrates, as shown, e.g., by Kluska . The $S_{eff,rear}$ thus sought is given by considering the SRV at the LCP surface S_{LCP} , which substitutes the contact SRV S_{cont} of Fischer's model, and the passivation SRV S_{pass} .

The method for rear side LCP samples, which is based on the measuring method described by Plagwitz to obtain S_{cont} from lifetime measurement for Fischer-like samples, is hereafter described, starting from some simple considerations.

- Lifetime measurements on the sample provide a value of τ_{eff} which takes into account both the SRV from the front and rear surfaces S_{front} and $S_{eff,rear}$, together with the bulk recombination:

$$\frac{1}{\tau_{eff}} = \frac{1}{\tau_{bulk}} + \left(\frac{W}{S_{front} + S_{rear}} + \frac{1}{D} X \right)^{-1} \quad (2.2.15)$$

$$\text{where (see 2.2.2.1) } X = \begin{cases} (W/\pi)^2 & \text{transient mode} \\ (W^2/12) & \text{quasi-steady state mode} \end{cases} .$$

The SRV of the whole sample S_{eff} is obtained from the measured τ_{eff} by

$$S_{eff} = \frac{W}{2} \left(\left(\frac{1}{\tau_{eff}} - \frac{1}{\tau_{bulk}} \right)^{-1} - X \right)^{-1} \quad (2.2.16)$$

where the bulk contribution can be neglected for high-quality bulk material samples.

- SRV on the rear side $S_{eff,rear}$ depends on the pitch L_p via the resistance terms R_s and R'_s .

$$S_{eff,rear} = \frac{D}{\left(\left(\frac{R_s}{\rho} + \frac{D}{fS_{LCP}} \right)^{-1} + \left(\frac{R'_s}{\rho} + \frac{D}{(1-f)S_{pass}} \right)^{-1} \right)^{-1} - W}$$

where the terms R_s and R'_s for the LCP lines and the passivated area respectively, are given an approximated expression, according to Plagwitz:

$$R_s = L_p^2 \frac{\rho}{2\pi r} \arctan \left(\frac{2W}{r} \right) + \rho W \left(1 - e^{-W/L_p} \right)$$

2 Experimental setup and characterization methods

$$R'_s = \left(\frac{1}{\rho W} - \frac{2\pi r}{\rho L_p^2 \arctan(2W7r) e^{W7L_p}} \right)$$

where ρ is the resistivity, r the line width and W the wafer thickness.

- Measuring S_{eff} for different sample designs, shown in Figs. 2.2.4, 2.5, 2.6, allows to obtain a measured value for the front SRV S_{front} and for the passivation SRV S_{pass} , thus enabling to calculate $S_{eff, rear}$ from measured S_{eff} by simple subtraction.

Together with the LCP samples, each with a different L_p , two symmetrical reference samples are then required for this measurement method, which is summarized as follows:

1. Reference probe with passivation layer only. (Fig. 2.2.4) The S_{eff} given by the

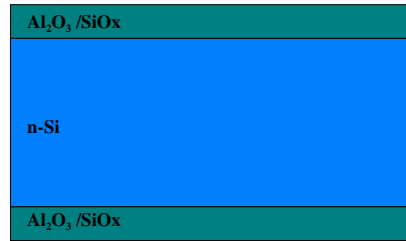


Figure 2.2.4: Fischer's method: reference probe for passivation

lifetime value τ_{eff} measured on this probe via the general expression 2.2.16 has the meaning of the S_{pass} for the sample general structure 2.2.6

$$S_{pass} = \frac{W}{2} \left(\left(\frac{1}{\tau_{eff}} - \frac{1}{\tau_{bulk}} \right)^{-1} - X \right)^{-1}$$

2. Reference probe with emitter layer under passivation. (Fig. 2.2.5) The S_{eff} given by the lifetime value τ_{eff} measured on this probe via the general expression 2.2.16 has the meaning of the S_{front} for the sample general structure 2.2.6

$$S_{front} = \frac{W}{2} \left(\left(\frac{1}{\tau_{eff}} - \frac{1}{\tau_{bulk}} \right)^{-1} - X \right)^{-1}$$

3. Test samples with passivation layer and emitter on the front and LCP lines on the rear (Fig. 2.2.6). The pitch between lines is different for each sample. The

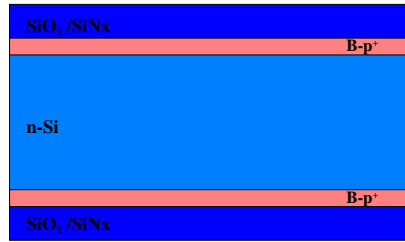


Figure 2.2.5: Fischer's method: front side probe

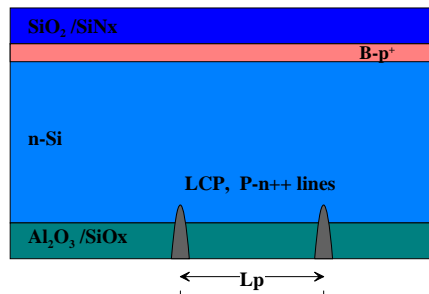


Figure 2.2.6: Fischer's method: reference probe for passivation

SRV S_{eff} given by the measured lifetime τ_{eff} via the Eq. 2.2.16, together with the value for S_{front} calculated from the second reference probe, give the rear SRV as a function of the pitch

$$S_{eff, rear} = \frac{W}{2} \left(\left(\frac{1}{\tau_{eff}} - \frac{1}{\tau_{bulk}} \right)^{-1} - X \right)^{-1} - S_{front} .$$

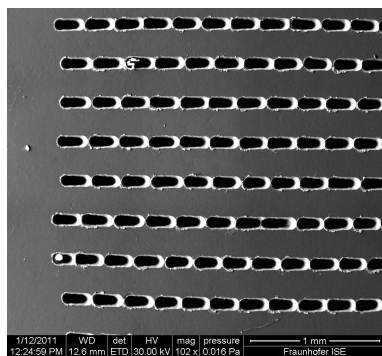
4. Fitting $S_{eff, rear}$ data as a function of L_p gives, as asymptotical values, S_{LCP} for $L_p \rightarrow 0$ and S_{pass} for $L_p \rightarrow L_{max}$, where L_{max} is the sample length in the direction perpendicular to that of line length . The fitting can be carried out by means of a script for Mathematica7.0 written at Fraunhofer ISE, either fixing the asymptotical value of S_{pass} to its measured value or leaving it as a freedom degree.

3 Deep grooving

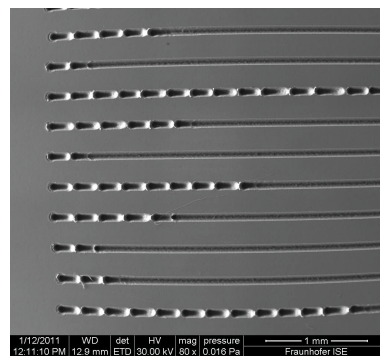
As discussed in Sec. 1.2, LaserChemicalProcessing can find its application either in cutting, e.g. for wafering, or in 2-D working to achieve selective doping of the silicon surface (up to depths of some μm) by means of diffusion in locally molten silicon.

If structures in the $100\mu m$ range are to be induced, then some unexpected irregularity in the grooves morphology arises, which is surely not acceptable for any of the LCP applications.

More in detail, it has been observed that, for some sets of parameters, the lines show periodical interruptions all along their length, as in Fig.3.0.1 .



(a) SEM image of an interrupted line, @ 200bar, 1.09mJ, 20mm/s



(b) SEM image of an interrupted line, @ 200bar, 0.366mJ, 6mm/s

Figure 3.0.1: Examples of interrupted LCP-processed grooves where the interruption is at the beginning (3.0.1a) or all along (3.0.1b) the line length

This chapter deals with a systematic study on the groove quality, evaluated in terms of reached depth and probability of generating interruptions, and is aimed at linking process parameters to groove morphology. Besides the general investigation of a new field of application for LCP, this analysis will be used to optimize the $150\mu m$ LCP

3 Deep grooving

grooving and can act as a reference to implement processes where different depths are to be reached.

The approach that has been followed is, first, to scan the effects produced by a wide range of process parameters and, secondly, to focus on achieving the depth of 150 μm with grooves that do not show any interruption-effect. A description of some technological details of applied processing can be found in Appendix B, at page 79.

3.1 Influence of process parameters on groove depth and continuity

Non coated, non textured, Boron *p*-type doped, FZ-monocrystalline silicon wafers of 10mm diameter were used for this investigation. A CNC programme was written to process 24 fields on a single wafer, each made of 20 parallel lines, as sketched in the figure in Appendix C at page 81. The line length was arbitrary fixed at 20 mm and the spacing between lines at 0,3 mm.

Each field was assigned a different set of parameters, so that the 20 lines are a small statistical sample for each set.

All the samples were processed with an 80 μm brass nozzle, using only water as a liquid medium and LEE laser system, which is the only one able to provide the required pulse energy to reach high grooving depth.

The range of values chosen for each parameter is summed up in Tab.3.1.1 .

Parameter			Values
<i>Press</i>	jet pressure	bar	{200;400}
<i>Freq</i>	pulse repetition frequency	kHz	{15;50}
<i>Lpow</i>	laser power	W	[18.3;60]
<i>SSp</i>	scanning speed	mm/s	[2;100]

Table 3.1.1: Range of parameters to study grooves processing with LCP

After the processing, the grooves depth and interruption probability were used as quantities to characterize each field. The value assigned to the groove depth of a field is an average over 8 values, measured by means of the confocal microscope Olympus

3.1 Influence of process parameters on groove depth and continuity

LEXT (see dedicated paragraph at page 32). To calculate the interruption probability $Int\%$, the ratio of the sum of the interrupted part of all the lines on one field over the sum of the line lengths

$$Int\% = \frac{\sum_1^{20} interrupted\ length_i}{\sum_1^{20} total\ line\ length_i}$$

was calculated for each field.

It is worth noting that for lines that show the interruption effect, the $Int\%$ assumes only values above 80% or under 35%, the former resulting from lines that are (almost)completely interrupted, the latter from lines only partially interrupted. In this second case, the lines look interrupted only at their beginning, as clearly visible in Figs. 3.0.1a and 3.0.1b.

3.1.1 First study on dependence of grooving quality on process parameters

A first test was carried out with the parameters¹ summarized in Tab.3.1.2, where three specific values for $Press$, $Freq$ and L_{pow} constitute a set of parameter. Each set is used to process six or more fields, each one with a different value for the Ssp in the range {2; 100}mm/s.

$Press$ [bar]	$Freq$ [kHz]	$InternalL_{pow}$ [W]	L_{pow} [W]	E_p [mJ]	Ssp [mm/s]
400	50	20	18.3	0.366	{2; 6; 10; 20; 50; 100}
	50	40	38.2	0.764	{2; 6; 10; 20; 50; 100}
	50	60	54.5	1.09	{2; 6; 10; 20; 50; 100}
400	15	40	38.2	2.55	{2; 6; 10; 20; 50; 100}
	15	60	54.5	3.63	{2; 6; 10; 20; 50; 100}
200	50	40	38.2	0.764	{2; 6; 10; 20; 50; 100}
	50	60	54.5	1.09	{2; 6; 10; 20; 50; 100}

Table 3.1.2: Parameters used for the first grooving test.

The results of depth measurement and interruption probability calculation were used to investigate the influence of parameters on groove depth, the occurrence of interrup-

¹The difference between $InternalL_{pow}$ and L_{pow} is due to absorption in the optical fiber (see5 and 2.1)

3 Deep grooving

tions with increasing depth and to check if a threshold depth exists for interruptions to occur. For the analysis of the results, L_{pow} and $Freq$ have been replaced by pulse energy E_p as a variable of interest, which allows to compare results obtained by different values of $Freq$, being $E_p \equiv L_{pow}/Freq^2$.

The following considerations, based on the results shown in Figs.3.1.1a, 3.1.1b, 3.1.1a, 3.1.1b, can be made:

- in the graph in Fig.3.1.1a the reached depth is plotted over Ssp for each set of parameters.

The logarithmic fit is in good agreement with data, the curve for each parameter set being part of a family of logarithmic curves $depth \sim -\ln(Ssp)$. A general tendency to shift upwards with increasing E_p for fixed $Press$ can be observed

- in the graph in Fig. 3.1.1b, interruption probability values $Int\%$ are plotted over depth without considering the process parameters. The aim is to highlight the possible existence of a threshold fixed depth, which would result in a step-like distribution.

This seems not to occur. Although, no interruption show up for depth lower than $100\mu m$

- in the graphs in Figs.3.1.1b and 3.1.1a, the values of $Int\%$ are plotted over the reached depth per each set of parameters.

The data evidence a peak-like or bell-like trend. The peak positions of the curves with the same $Press$ seem to shift according to L_{pow} mainly. This is intuitively understandable by the increasing L_{pow} allowing to reach higher depths. Note that these statements are justified by the fact that for each different set of parameters, Ssp was given always the same discrete set of values, namely $\{2; 6; 10; 20; 50; 100\}$ mm/s. Otherwise, no comparison could be made³.

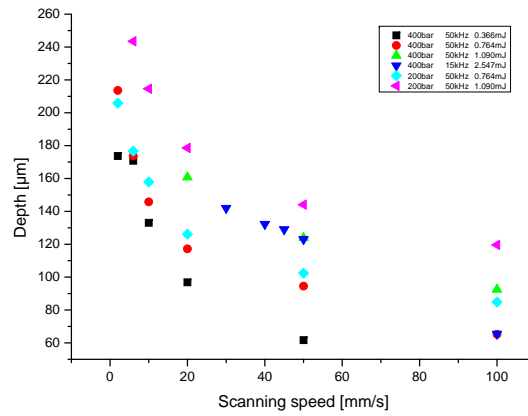
Comparison between graphs in Figs.3.1.1b and 3.1.1a shows that higher $Press$ induce a wider field of interruption occurrence, thus suggesting to prefer lower values for a good quality processing.

Moreover, some further considerations can be made by means of images obtained by LEXT:

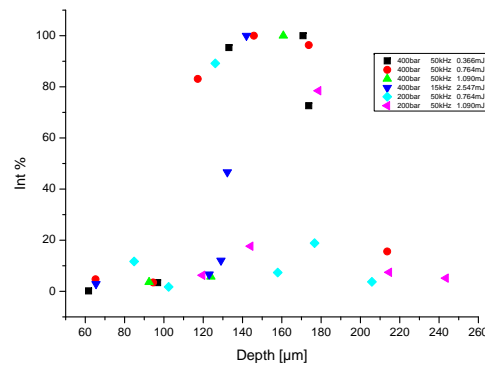
²Results obtained with the same pulse frequency can be equivalently compared either in terms of E_p or L_{pow} .

³Some data are missing in the graphs, mostly for some slow values of Ssp . This is due to the fact that some parameters caused the grooves to be through the wafer and therefore no value of depth can be plotted

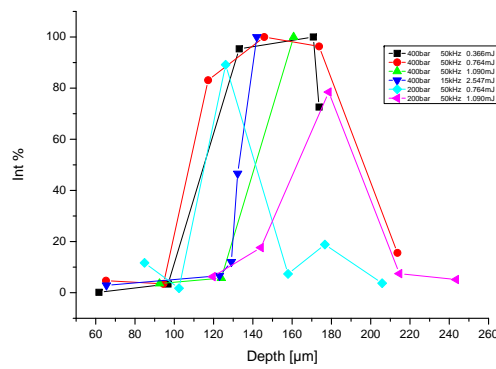
3.1 Influence of process parameters on groove depth and continuity



(a) Depth as a function of scanning speed

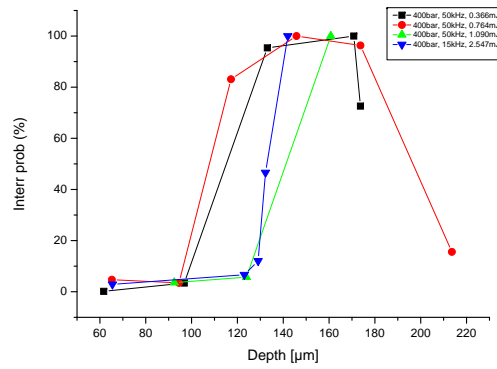


(b) Interruption probability over depth

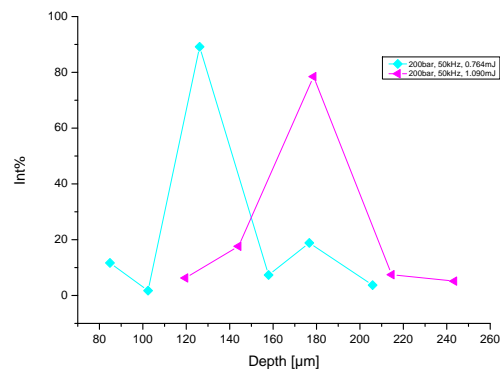


(c) Interruption probability over depth (lines connect values obtained with the same S_{sp})

3 Deep grooving



(a) Interruption probability over depth @400bar



(b) Interruption probability over depth@200bar

3.2 Optimizing the 150 μ m-depth grooving

- the fields processed with $Freq = 15\text{kHz}$ and $Press = 400\text{bar}$ are often cut through or show lines with very irregular groove surfaces. Then, further investigation with this couple of parameters seems not to be convenient.
- processing with high values of Ssp reduces, on the one hand, the occurrence of interruptions (see graph in Fig3.1.1b , where $Int\%$ is plotted on Ssp), but on the other hand turns out into grooves with some irregular bottom profile.

3.1.2 Interruptions features

LEXT microscope was used to characterize the interrupted grooves.

Cross-section images were taken at half the groove width, with a crossing-plane perpendicular to the wafer surface. A saw-teeth shape of the processed area is shown, both for $Int\%$ below 35% or above 80% (see Fig.3.1.1)

Periodicity Planar images on the wafer surface plane were taken for the fields which $Int\%$ is above 80% (see Fig.3.1.2) . These were then used to measure the period of the interruptions. No correlation was found between the interruption period and any process parameter.

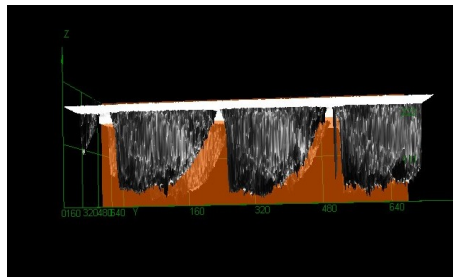
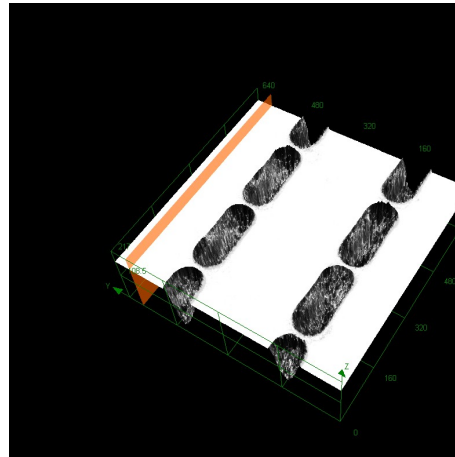


Figure 3.1.1: LEXT image of an interrupted groove cross section, @400bar, 0.7764mJ, 10mm/s . The orange sectioning plane highlights the saw-tooth shape of the interruption cross section

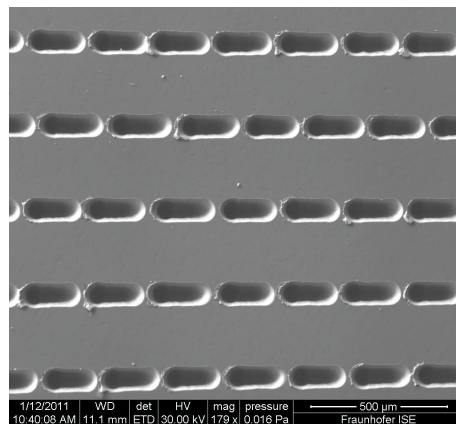
3.2 Optimizing the 150 μ m-depth grooving

On the basis of the previous statements, the criterion to choose the parameters to optimize the 150 μ m-grooving and further investigate the interruption effect goes in

3 Deep grooving



(a) LEXT image of periodical interruptions on a field, @400bar,0.7764mJ, 10mm/s



(b) SEM image showig periodical interruptions, @400bar, 0.366mJ, 10mm/s

Figure 3.1.2: SEM and LEXT images showing interruption periodicity

3.2 Optimizing the 150 μ m-depth grooving

the direction of

- a) using low *Press* , namely 200bar ;
- b) try to shift the two curves in Fig.3.1.1b by changing L_{pow} , in order to make the 150 μ m depth be on the tails of the curves and
- c) check if the same conclusions of non-sufficient process quality for $Freq = 15kHz$ are reached also with a different value of *Press*, namely, 200bar.

Then, some new fields were processed with the parameters in Tab. 3.2.1

<i>Press</i> [bar]	<i>Freq</i> [kHz]	<i>Internal</i> L_{pow} [W]	L_{pow} [W]	<i>Ssp</i> [mm/s]
200	50	20	18.3	{2; 6; 10; 20; 50; 100}
200	50	30	27.0	{2; 6; 10; 20; 50; 100}
200	50	64.5	59.9	{2; 6; 10; 20; 50; 100}
200	15	20	18.3	{2; 6; 10; 20; 50; 100}
200	15	40	38.2	{2; 6; 10; 20; 50; 100}

Table 3.2.1: Parameters used for further grooving test

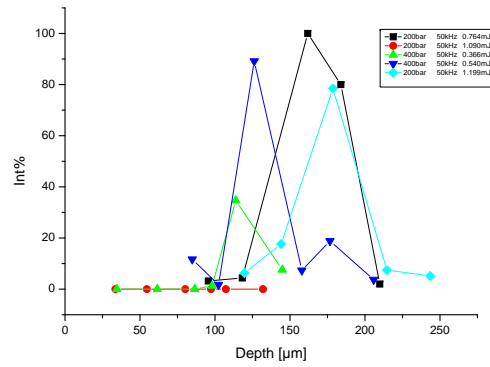
The results of these new tests are summarized in the graphs of Figs. 3.2.1a and 3.2.1b, where the new data are plotted together with those coming from the same couple (*Press*; *Freq*) of the first test.

Together with grooves images taken with the LEXT microscope, these results allow the following overall conclusions:

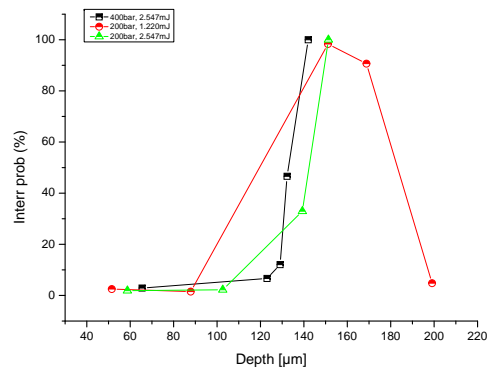
- Processing with 15kHz pulse frequency does not give acceptable results. The interruption occurrence seems to be increased and even when this does not happen, the output grooves appear to have very irregular surfaces, even the shallower ones. This often causes micro-cracking in the unprocessed area between the lines, that turns out into wafer breaking.
- Processing with 50kHz pulse frequency gives promising results in term of grooves regularity, both in their continuity and cross-sectional surface regularity, especially if a jet prssure of 200bar is applied. Moreover, the process stability and controllability seem to be enhanced.

By choosing suitable couples (L_{pow} , *Ssp*), different depth can be reached with a process that grants good continuity and regularity.

3 Deep grooving



(a) Interruption probability over depth for $Press = 200bar$ and $Freq = 50kHz$



(b) Interruption probability over depth for $Press = 200bar$ and $Freq = 15kHz$

Figure 3.2.1: Graphs of results from second grooving test

3.3 Conclusions

- For the scope of optimizing the $150\mu m$ -grooving, the best results are obtained with

$Press$ [bar]	$Freq$ [kHz]	L_{pow} [W]	Ssp [mm/s]
200	50	27.0	2

or, equivalently,

$Press$ [bar]	E_p [mJ]	Ssp [mm/s]
200	0.54	2

which allow to obtain a depth of $132\mu m$. This is not so far from the depth sought, but requires a slow Ssp , that might be not suitable for a successive industrial application in solar cell production.

On the basis of the previous statement, another approach was applied to make the deep-grooving feasible, that is, to process one line with more than one scanning pass. This solution was not considered before, because some not systematic tests, carried out before this work, had led to unsatisfactory results. The choice of the parameters to apply was made possible by the overall analysis previously described, which allows to make accurate esteems on the expected results. The relevant data and results are collected in Tab.3.2.2 and Fig. 3.2.2. All the grooves processed with multi-pass mode show no interruption effect.

$Press$ [bar]	$Freq$ [kHz]	L_{pow} [W]	E_p [mJ]	Ssp [mm/s]	N of passes	$Depth$ [μm]
200	50	27.0	0.54	20	2	176.95
200	50	18.3	0.37	50	2	151,39

Table 3.2.2: Relevant data for grooves processed with multi-pass mode

3.3 Conclusions

The grooving tests described before have improved the understanding of the relationship between groove quality and process parameters, the pulse energy E_p being the most relevant one.

3 Deep grooving

For fixed E_p , decreasing the scanning speed Ssp allows to groove deeper, as can intuitively be understood.

The pulse frequency $Freq = 15kHk$, even at the lowest value of L_{pow} induces a high pulse energy E_p to be deposited on the wafer surface, which often results in wafer cutting or cracking.

A possible explanation for the interruption effect could arise from fluid dynamics and optical considerations. The high E_p required for deep grooving induces silicon evaporation, which causes a recoil pressure to be exerted on the molten silicon surface. This, together with the jet pressure that impinges on the target surface, causes a turbulent molten silicon movement. The bifasical flow of molten silicon and water jet thus originated could be responsible for breaking the jet laminarity, thus inducing the laser light to be guided no more and be lost outside the jet. In addition, the shield effect of a pulse-induced silicon vapour on the successive pulses has to be considered, especially for those couples ($Freq$, Ssp) that generate the highest pulse overlap (see Appendix A, at page 77). These two effects turn out into a non spatially uniform, oscillating, jet interaction with silicon surface, which originates the saw-teeth shape.⁴

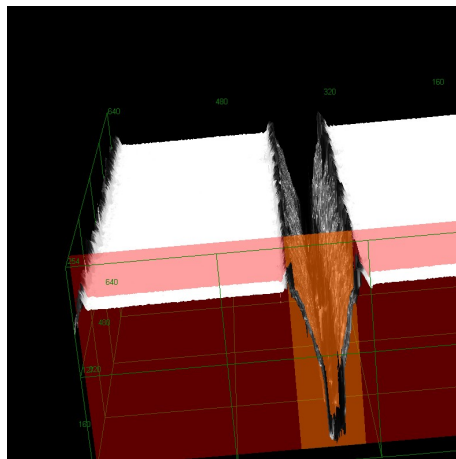
Another possible explanation is a pure “geometrical oscillation”. The jet is “trapped” in the currently ablating hole and is “bent” while moving in scan-direction. At a critical depth and/or bending angle, the jet flips out to a new position and starts to form a new hole. The “trapping effect” works only at a significant depth.

Still it is not clear the reason why in some cases the interruptions are set at the begin of a line and disappear at some later point, as if the corresponding parameters could set a sort of turning point between the stability represented by continuous lines and the instability of periodical interrupted ones. Obviously, the oscillation effect is induced at the beginning and can be dumped during scanning

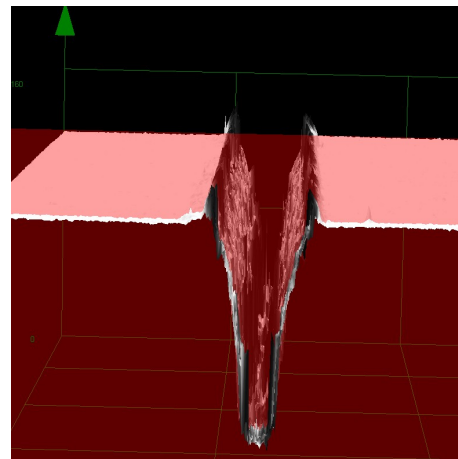
Deep grooving opens thus new possibilities for further investigation and modeling on physical effects induced by LCP, especially at high pulse energy regimes.

⁴For a detailed analysis of fluid dynamics and thermodynamics effects induced by LCP, see [4]

3.3 Conclusions



(a) @200bar, 50kHz, 0.54mJ, 20 mm/s. The orange plane highlights the groove section.



(b) @200bar, 50kHz, 0.37mJ, 20 mm/s. The orange plane highlights the groove section.

Figure 3.2.2: LEXT images of grooves obtained with multipass mode

4 Doping while shallow grooving

One of the most promising applications for LCP is local doping (see Sec.(1.2)). At the state of the art, the doping process via LCP is used to produce highly-doped lines on the silicon surface (depth $\leq 5\mu m$) with either n -type or p -type dopant media . Since low pulse energies E_p are required to break the passivation layer and locally melt silicon without ablation, the HIPPO laser system is usually employed. Typical parameters for the n -type doping process of such kind, later on referred as “standard doping LCP”, are summarized in Tab. 4.0.1 [13].

<i>Liquid jet</i>	<i>Nozzle diameter</i>	<i>Press</i>	<i>Freq</i>	L_{pow}	E_p	S_{sp}
	[μm]	[<i>bar</i>]	[<i>kHz</i>]	[<i>W</i>]	[<i>mJ</i>]	[<i>mm/s</i>]
H_3PO_4 (85% aqueous sol.)	50	160	35	0.6	0.0120	50

Table 4.0.1: Parameters for standard doping LCP

As stated in Sec. 1.3, the possibility to match the LCP doping task with the 3-D structuring one is investigated in this chapter.

Together with the processing and characterization techniques of standard doping LCP, the study described in Chap.3 will be used as a starting point for the work in this chapter. The aim is to evaluate the feasibility of doping while grooving, on the basis of laser-induced damage in Si crystal lattice and doping quality¹. The quantity the assessment is based on is the surface recombination velocity (SRV)².

¹The generical term “doping quality” takes into account depth of doping, doping concentration and doping homogeneity both spatial and chemical. A rigorous quantitative analysis is out of the scopes of this work.

²For a deeper insight into the relation of doping and SRV, see [2]

4.1 Short qualitative description of H_3PO_4 -grooving induced effects

If LCP is applied with phosphoric acid H_3PO_4 and enough E_p to produce a groove in tenth of μm depth range, the following effects are expected to be induced and to influence the SRV.

Creation of high SRV surface The laser causes the passivation layer to be opened and a new unpassivated surface to be created, that is, the groove surface. The SRV is expected to dramatically increase, the increment being strongly influenced by the amount of new unpassivated surface created. Thus, the geometrical variables related to the groove shape (i.e., depth, cross sectional profile and surface roughness) have an important role.

Crystal lattice damage Compared to dry laser ablation, LCP induces lower damage in the target silicon [12, 20], mainly because the thermal stresses are reduced by high-temperature molten silicon ablation. Nonetheless, the silicon volume surrounding the groove surface has to be considered as a high recombination area. Here, the recrystallized silicon is still in monocrystalline form, but includes a lot of defects (impurities inclusion and dislocations), thus presenting a higher amount of recombination centers. Moreover, the underlying heat-affected zone will show crystal lattice distortion induced by thermal stresses. The amount of volume involved in such phenomena depends mainly on the *fluence*, that is, deposited energy per unit area³, and on the time scale involved, which is determined by the pulse duration $\Delta\tau_{pulse}$.

Surface field passivation (and shielding) effect A heavily doped surface region is shown to induce a passivation effect on bulk of the same doping type [9], because of the potential barrier set by the the Fermi level shifting towards the edges of the bandgap due to heavy doping [34]. Intuitively, carriers with charge of the same sign as those in the heavily doped region are kept away from the surface, thus decreasing the SRV. This field effect passivation is strictly dependent on doping quality,

³All the experiments here presented have been carried out with the same nozzle and then the laser spot area assumes always the same value. This will allow the use of E_p instead of *fluence* for the later discussion.

4.2 Evaluation of SRV for different LCP paths

defined in terms of doping concentration absolute value, spatial profile in the direction perpendicular to the groove surface⁴ and spatial homogeneity of doping profile in the direction of the groove length.

For LCP, the resulting doping may this way shield the damaged region from minority carriers, reducing effectively the SRV and making it suitable for solar cell applications.

4.2 Evaluation of SRV for different LCP paths

Samples were processed with the two available 532nm laser systems, HIPPO and LEE, which differ mainly for the induced pulse duration $\Delta\tau_{pulse}$.

For each laser system, the pulse frequency $Freq$ was given a fixed value : 50kHz for LEE⁵ and 15kHz for HIPPO⁶.

E_p and $Press$ were varied⁷ to study the related change in induced SRV.

Process parameters were chosen to give, as far as possible, always the same groove depth and surface shape, in order to minimise the influence of geometric variables on SRV. This was achieved by according Ssp to L_{pow} in order to reach a depth of $\simeq 20\mu m$.

4.2.1 Selecting parameters on the basis of QSSPC-measured lifetime

A first test was conducted on Cz-boron doped wafers, passivated on both sides by a SiO_2 , 100nm-thick layer. 28 fields of parallel grooves were processed, each one with a different set of parameters. The pitch between lines L_p was the same on all the fields. Tab. 83 in the Appendix at page 83 summarizes the used parameters, which were chosen, at this stage, to scan a wide range of E_p ⁸.

⁴Due to the peculiarity of doping with LCP towards the usual doping method by vapour diffusion, it is reasonable to expect a non-homogeneous doping profile on the groove cross section plane for points at the same distance from the groove surface

⁵see discussion in Chap.45

⁶For this pulse frequency it is possible to reach the maximum power.

⁷Being $Freq$ fixed, E_p is varied only by changing L_{pow}

⁸For HIPPO laser, E_p value goes from slightly above the standard doping process to the maximum allowed.

4 Doping while shallow grooving

This first test was aimed at choosing some relevant parameters for further investigation to be conducted by means of the Fischer/Plagwitz method described in 2.2.2.2. The choice was based on a comparison between the minority carrier lifetimes τ_{eff} obtained for each field by QSSPC measurement.

The results of τ_{eff} are plotted over the pulse energy E_p in Graph. 4.2.1, where a well separate behaviour for the two laser systems is highlighted. Lifetime data referred to LEE show a very low sensitivity on E_p , while for HIPPO lifetime is rapidly decreasing with increasing E_p . The jet pressure seems not to be a relevant parameter.

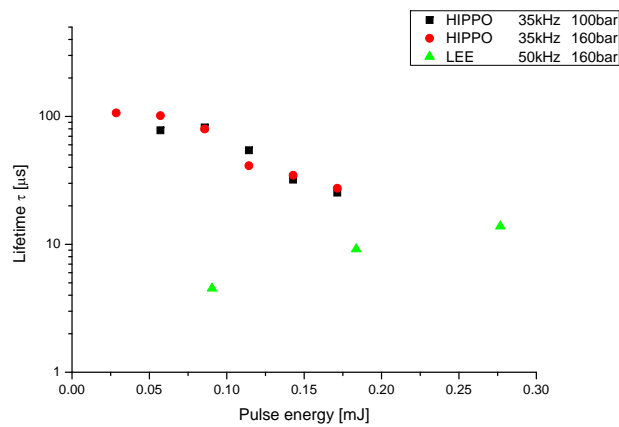


Figure 4.2.1: Effective lifetimes measured by QSSPC are plotted, on a logarithmic scale, as a function of the pulse energy

4.2.2 Applying Fischer/Plagwitz method to evaluate SRV induced by H_3PO_4 -grooving LCP

SRV measuring method by Fischer and Plagwitz has been used to calculate SRV of standard LCP doped lines ($\leq 5\mu m$) [19].

The application of the same method to our case requires some attention. If grooves are produced instead of just superficial lines, the implicit hypothesis of flat rear surface, which Fischer's model is based on, stands no more. The error introduced is to calculate the fraction f of the LCP-processed surface on the basis of its projection

4.2 Evaluation of SRV for different LCP paths

on the rear surface plane. This approximation is acceptable in the case under exam, where the groove depth is $\simeq 20\mu m$ and its width $\simeq 40\mu m$ and the pitch L_p assumes the values $\{500; 1000; 1500; 2000; 3000; 6000\}\mu m$. This means that, even in the worst case of rectangular groove shape, the open surface underestimation is $\leq 40\mu m$. Comparing this value with the minimum pitch $L_p = 500\mu m$ gives evidence that the error induced in the esteem for f is tolerable. In our analysis, the line width that enters the Fischer/Plagwitz-model will be the projected one. Then, the results thus obtained are assumed to state upper limits of SRV.

FloatZone, n -type wafers were used for the Fischer/Plagwitz SRV measurement technique. The wafers to be processed by H_3PO_4 -LCP have a p^+ -Boron diffused layer underneath an Al_2O_3/SiO_x passivation layer on the front side and a SiO_2/SiN_x passivation layer on the back side (see Fig.4.2.2c).

In addition, as required by the experimental scheme (see Pag.42), two reference samples were prepared, the one for the SRV of the rear side oxidation and the other for the front side emitter and passivation layers.(see Figs. 4.2.2band 4.2.2a) .

The parameters used for the LCP were selected on the basis of the previous test and are summarized in Tab.4.3.1 and an example of a processed wafer is in Fig.

One set of parameters per each laser system was chosen to carry out processing not only with H_3PO_4 but also with H_2O . This was aimed at allowing a simple comparison between the two cases, the one with water involving only crystal damage and surface opening effects, the one with H_3PO_4 also doping-induced effects.

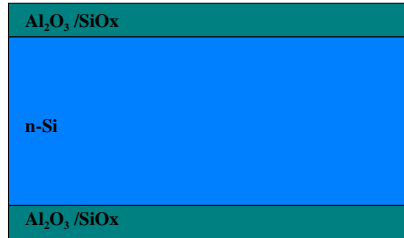
Nevertheless, this does not mean that an accurate separation between the grooving-induced and doping- induced effects can be made, since the phenomena occurring at the silicon surface are not the same if H_3PO_4 is used instead of H_2O ⁹.

Each set of parameters was used to process six different fields, each one with a different value for the pitch L_p belonging to $\{500; 1000; 1500; 2000; 3000; 6000\}\mu m$. Afterwards, a lifetime value τ_{ef} was obtained for each field via QSSPC measurement, as well as for the reference samples.

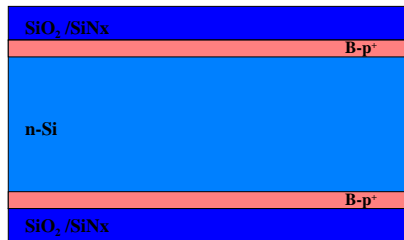
The data thus obtained were elaborated by means of a script for Mathematica7.0 written by Kluska and Cinkowsky at Fraunhofer ISE. The script introduces the τ_{eff} and L_p data in Fischer/Plagwitz calculation and returns a SRV value for each pitch.

⁹For example, different rheology determined by the highly different viscosity.

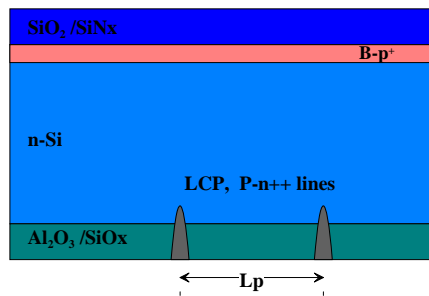
4 Doping while shallow grooving



(a) Fischer's method: reference probe for passivation



(b) Fischer's method: front side probe



(c) Fischer's method: reference probe for passivation

Figure 4.2.2: Sketch of reference and processed samples according to Fischer/Plagwitz scheme

By fitting the SRV values over the pitch, it gives the final SRV of the LCP area as asymptotical value (see Par. 2.2.2.2). A graphic example of the script output is given in Fig. 4.2.4, referred to a LEE-processed sample where $E_p = 0.1836 \text{ mJ}$.

4.3 Results and Conclusions

The final results for the SRV are given in Tab. 65 and in Fig.68 and allow the following conclusions.

Laser system	$H_3PO_4^{10}$	Nozzle diameter	Press	Freq	L_{pow}	E_p	S_{sp}	SRV
HIPPO/LEE	0/1	[μm]	[bar]	[kHz]	[W]	[mJ]	[mm/s]	[cm/s]
HIPPO	0	50	160	35	2.00	0,0571	25	36802,14
HIPPO	1	50	100	35	2.00	0,0571	25	14488,24
HIPPO	1	50	160	35	0.60	0,0171	50	12040,63
HIPPO	1	50	160	35	2.00	0,0571	25	10319,70
HIPPO	1	50	160	35	4.00	0,1143	35	46434,63
LEE	0	50	160	50	4.53	0,0905	40	486282,87
LEE	1	50	160	50	4.53	0,0905	40	3582,62
LEE	1	50	160	50	9.18	0,1836	50	3451,33
LEE	1	50	160	50	13.84	0,2768	100	3103,48

Table 4.3.1: SRV results from lifetime QSSPC data elaborated by means of a Mathematica7.0 script written at Fraunhofer ISE.

- The jet pressure is confirmed not to be highly relevant, at least for the HIPPO laser.
- If the two H_2O samples are compared each with its analogous with H_3PO_4 , a very strong increase in SRV in the water case is observed, which is of big interest for two reasons. First, it proves that doping has been achieved by LCP while grooving. Second, it gives a strong evidence that this doping layer exerts effectively a recombination“shield” effect by surface field passivation.
- The two behaviours for HIPPO and LEE are clearly separate and can be directly compared for the values of E_p around $0,1 \text{ mJ}$. In general, the SRV absolute values are much higher for HIPPO than for LEE. What is changing between the two laser system is the pulse duration $\Delta\tau_{pulse}$, which appears then to be of great importance.

4 Doping while shallow grooving

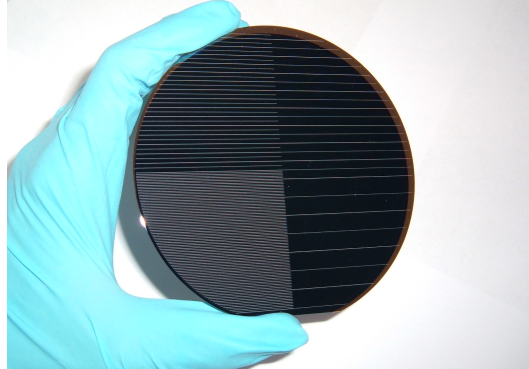


Figure 4.2.3: An example of a wafer processed by LCP. The four fields are processed each with a different pitch

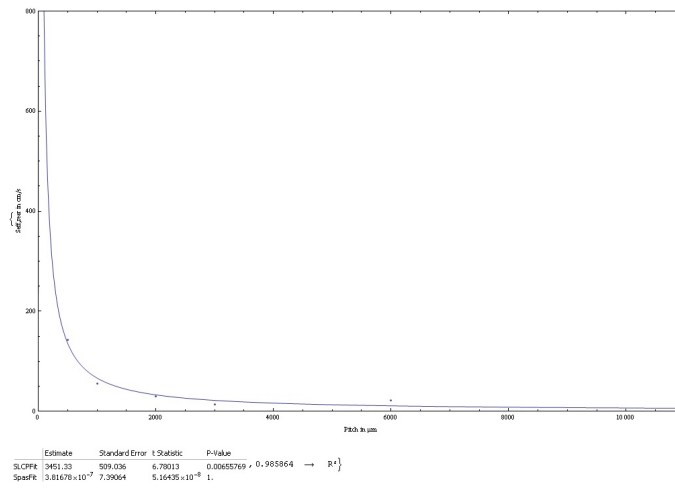


Figure 4.2.4: An example of a fit curve of SRV on pitch, given by the Mathematica 7.0 script.

4.3 Results and Conclusions

A possible non-rigorous explanation for the results obtained can be formulated by considering the two totally different values of $\Delta\tau_{pulse}$ for the two laser systems. If HIPPO laser is used for processing, $\Delta\tau_{pulse} \sim 10ns$, while for LEE $\Delta\tau_{pulse} \sim 400ns$. This turns out in the target response to be different in the two cases.

In the short pulse regime of HIPPO, the volume affected by thermal effects is confined mostly to the spot region. The amount of silicon involved in melting and recrystallization is then limited. On one hand, this translates into a smaller volume interested by doping, since doping via LCP is induced only in molten silicon¹¹. On the other hand, the thermal confinement determines small crystal damage, which is caused by the short pulse induced shockwave.

In the long pulse regime of LEE, a higher amount of silicon is melted and melt flow cannot be neglected. Then, a volume much deeper than for the short pulses is involved in heat transport phenomena and more crystal damage is globally induced. However, the higher amount of silicon melted and the longer time scale reasonably turn out into a deeper doping penetration and in a higher dopant concentration. Moreover, in the region below the melt, the thermal gradients generated by long pulse duration are lower than for short pulse durations. This induces less thermal stress, that is less severe crystal damage.

Standing these considerations, the fact of SRV being definitely higher for HIPPO than for LEE for similar E_p , means that enhancement in doping quality induced by longer pulses is as strong as to overcompensate the increased damage.

However, the SRV for standard doping process seems too high, so the absolute values should be taken with care.

Finally, SRV values obtained by means of LEE processing are absolutely acceptable for solar cells application, being comparable to the reference values of SRV for standard passivated emitters ($SRV \sim 3000cm/s$).

¹¹The diffusion constant in solid silicon is several order of magnitude less than in molten silicon

4 Doping while shallow grooving

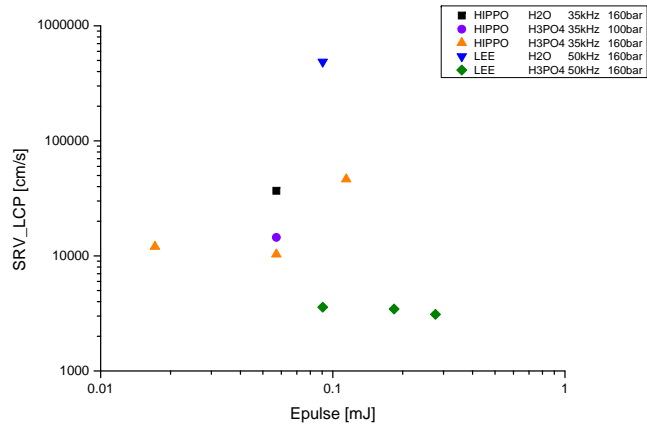


Figure 4.3.1: SRV is plotted in bilogarithmic scale as a function of pulse energy

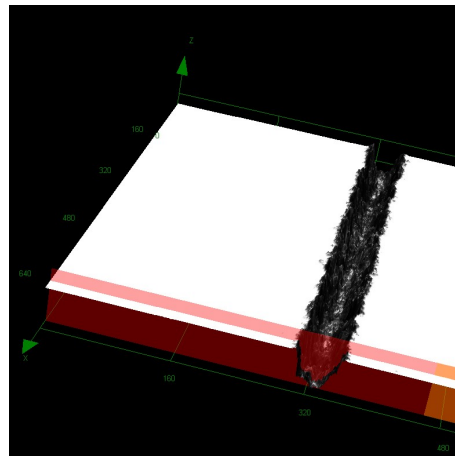


Figure 4.3.2: LEXT image of a doped groove obtained with a LEE laser processed field (@160bar, 0.2768mJ, 100mm/s) where the pitch is $3000\mu\text{m}$

5 Summary

The aim of this work was to carry out a study on some criticalities that arise if grooving and doping with LCP are combined .

In the introduction, after a short description of the main features of a silicon solar cell , an overview on LCP describes the main phenomena occurring in the jet and at the target surface, as well as the main fields of application.

After presenting the experimental setup used for LCP, some characterization methods are described in Chapter 2 as, for example, optical confocal microscopy by means of LEXT.

The main theoretical background and technological features of lifetime measuring via Quasi-Steady-State-PhotoConductance (QSSPC) are outlined, together with the detailed description of the measuring method by Fischer and Plagwitz for the surface recombination velocity calculation.

Chapter 3 is dedicated to the study on the grooving task alone. Samples have been processed with water as a liquid medium, wherein LEE laser were coupled by means of a nozzle of $80\mu m$ diameter. The main goal was to find a relation between process parameters and grooving features, which could constitute a basis for further process optimization for a given depth.

The pulse energy E_p is found to be the parameter which the reached depth is mostly depending on, together with the scanning speed Ssp . This is reasonable, since the pulse energy, together with the pulse duration (that is fixed for a given E_p), determines the amount of the silicon that is melted and/or evaporated and can thus be ablated.

Additionally, the lower value for the pulse repetition rate, $Freq = 15kHz$, is shown to often induce wafer breaking or irregular groove borders. An explanation for this is coming from the fact that low frequencies give high pulse energy through the relation

5 Summary

$E_p = L_{pow}/Freq$. This high E_p induces mechanical stresses in the silicon target by means of tensile waves and induces a sort of spallation mechanism.

If depths $\geq 100\mu m$ are sought, a sort of instability effect is observed, that is, grooves show periodical, saw-teeth cross sectioned interruptions, the period being not related to any process parameter. A probability of the interruption effect occurrence $Int\%$ has been defined and its variation studied as a function of depth for the sets of parameter under observation.

A possible explanation is seen in the optics and fluid dynamics phenomena that take place if a high- E_p interaction with the target is set. Here, in contrast with the case of low E_p , a molten silicon movement could be set, which the jet and the unnegligible recoil pressure concur in. Moreover, the presence of silicon vapour within the groove could have an impact, both by means of a recoil pressure and of a shielding effect, that cannot be ignored. However, the complex interaction of fluid dynamics and thermal phenomena that cause the physical “oscillation effect” is still to be investigated.

The results obtained are finally used in the perspective of optimizing grooving process for $150\mu m$ target depth. A precise, versatile and time-saving way was identified in multipass-mode. For the aim of $150\mu m$, good quality grooving was achieved by $Press = 200bar$; $Freq = 50kHz$; $E_p = 0.37mJ$; $SSP = 50mm/s$.

In Chapter 4 grooving and doping are joined for the very first time. The aim is to conduct a first investigation on the impact of the higher pulse energies required by grooving on the generated doping quality.

The most critical points to verify are the damage induced by high E_p and the effective presence of a doped layer underneath the groove surface. For this scope, the QSSPC characterization technique has been chosen. Since the lifetime is dramatically decreased if a non passivated surface is present, and the non passivated area is strictly connected to the groove geometrical features, the experiment are designed to minimize the groove depth and shape variation.

Both the two laser systems, the HIPPO typically used in doping process and the LEE, which maximum power allows also cutting applications, are considered, so that to allow a final comparison. Samples are processed with H_3PO_4 to induce n -type doping.

A first test is carried out to have a first rough understanding on the lifetime dependence on process parameters. The results are used to choose some relevant parameters for the successive investigation, to be conducted within the surface recombination velocity measurement scheme described by Fischer and Plagwitz. By means of comparing the SRV (obtained by QSSPC measurement) of reference samples with the SRV of samples where lines are processed with varying pitches, the SRV for the processed surface is calculated.

Importing the Fischer/Plagwitz experimental technique, which is based on the implicit assumption of flat processed surface, is allowed by a geometrical consideration. The absolute error introduced in considering the groove projection surface instead of the 3D effective open surface is small compared to the smallest pitch. Further, the analysis is carried out in such way that the resulting SRV can be seen as an upper limit to the actual SRV.

From the SRV results, a very different behaviour is observed between LEE and HIPPO, both in trends and absolute values. The HIPPO SRV values are generally higher than LEE ones, even though the longer pulse duration of LEE is supposed to induce more crystal damage. This can be explained by an enhanced doping quality, in terms of depth of penetration and dopant concentration, which overcompensates the increased lattice damage by means of a field effect passivation.

The evidence that doping has been effectively induced while grooving is given by the comparison with the two samples processed with water, which show a definitely higher SRV (up to two orders of magnitude in the case of LEE laser).

The results thus obtained confirm the feasibility of grooving and doping processes to be carried out at the same time by means of LCP. The achievement of SRV in the range of 3000cm/s (that is comparable to the standard passivated emitter references) makes the process very promising for solar cells applications.

Proceedings could be done, e.g., by rigorously considering the physical effects occurring for the high pulse energy regimes (this is already being investigated by the LCP research group). Moreover, further characterizing could be, e.g., carried out to study the doping concentration profiles around the groove surface. Finally, if doped grooves deeper than the $20\mu\text{m}$ here considered are to be processed and investigated, an extension to Fischer's model needs to be developed which takes into account the 3D charge transport around the groove surface.

Bibliography

- [1] P. Couty, F. Wagner, and P. Hoffmann. Laser coupling with a multimode water-jet waveguide. *Optical Engineering*, 44(6):068001–1–8, 2005.
- [2] A. Cuevas, P. A. Basore, G. Giroult-Matlakowski, and C. Dubois. Surface recombination velocity of highly doped n-type silicon. *Journal of Applied Physics*, 80(6):3370–5, 1996.
- [3] Kristine Drew. Silicon solar cells: Combining laser chemical processing (lcp) and aerosol jet printing (ajp) for industrially relevant high efficiency front side structures. Master’s thesis, Ecole Polytechnique de Louvain, Université Catholique de Louvain, 2009.
- [4] A. Fell. *Modelling and simulation of Laser Chemical Processing (LCP) for the manufacturing of silicon solar cells*. PhD thesis, Universitaet Konstanz, 2010.
- [5] A. Fell and G. P. Willeke. Fast simulation code for heating, phase changes and dopant diffusion in silicon laser processing using the alternating direction explicit (ade) method. *Applied Physics A*, 98(2):435–440, 2009.
- [6] B. Fischer. *Loss Analysis of Crystalline Silicon Solar Cells using Photoconductance and Quantum Efficiency Measurements*. PhD thesis, Universitaet Konstanz, 2003.
- [7] F. Granek, M. Hermle, C. Reichel, A. Grohe, O. Schultz-Wittmann, and S.W. Glunz. Positive effects of front surface field in high-efficiency back-contact back-junction n-type silicon solar cells. 2008.
- [8] Filip Granek. High-efficiency back-contact back-junction silicon solar cells. 2009.
- [9] M. A. Green. *Solar cells: Operating principles, technology, and system applications*. 1982.
- [10] R. N. Hall. Electron-hole recombination in germanium. *Phys. Rev.*, 87(2):387, Jul 1952.

Bibliography

- [11] Christiana Honsberg and Stuart Bowden. <http://www.pveducation.org/pvcdrom>. website.
- [12] S. Hopman, A. Fell, K. Mayer, M. Aleman, M. Mesec, R. MÄCeller, D. Kray, and G. P. Willeke. Characterization of laser doped silicon wafers with laser chemical processing. In *Proceedings of the 22nd European Photovoltaic Solar Energy Conference*, pages 1257–61, Milan, Italy, 2007.
- [13] S. Hopman, A. Fell, K. Mayer, C. Fleischmann, D. Kray, and F. Granek. Study on laser parameters for silicon solar cells with lcp selective emitters. In *24th European Photovoltaic Solar Energy Conference*, Hamburg, 2009.
- [14] S. Hopman, A. Fell, K. Mayer, M. Mesec, A. Rodofili, and D. Kray. Comparison of laser chemical processing and lasermicrojet for structuring and cutting silicon substrates. *Applied Physics A*, 95:857–866, 2009.
- [15] S. Hopman, A. Fell, K. Mayer, M. Mesec, G.P. Willeke, and D. Kray. First results of wafering with laser chemical processing. In *Proceedings of the 23rd European Photovoltaic Solar Energy Conference*, pages 1131–5, Valencia, Spain, 2008.
- [16] S. Hopman, A. Fell, K. Mayer, A. Rodofili, and F. Granek. Microstructuring and wafering of silicon with laser chemical processing. In *Laser-based Micro- and Nanopackaging and Assembly IV*, volume 7585, San Francisco, 2010. SPIE.
- [17] Sybille Hopman, Kuno Mayer, Andreas Fell, Matthias Mesec, and Filip Granek. Laser cutting of silicon with the liquid jet guided laser using a chlorine-containing jet media. *Applied Physics A; Materials Science; Processing*, 102:621–627, 2011. 10.1007/s00339-010-6155-5.
- [18] S. Kluska, F. Granek, M. RÄEdiger, M. Hermle, and S.W. Glunz. Modeling and optimization study of industrial n-type high-efficiency back-contact back-junction silicon solar cells. 2010.
- [19] S. Kluska, A. Rodofili, K. Mayer, C. Fleischmann, F. Granek, and S.W. Glunz. Analysis of local boron dopings formed with lcp. In *25th European Photovoltaic Solar Energy Conference and Exhibition*, Valencia, Spain, 2008.
- [20] D. Kray, M. Aleman, A. Fell, S. Hopman, K. Mayer, M. Mesec, R. MÄCeller, G.P. Willeke, S.W. Glunz, B. Bitnar, D.H. Neuhaus, R. LÄEdemann, T. Schlenker, D. Manz, A. Bentzen, E. Saunar, A. Pauchard, and B. Richerzhaben. Laser-doped silicon solar cells by laser chemical processing (lcp) exceeding 202008.

- [21] D. Kray, A. Fell, S. Hopman, K. Mayer, S. Glunz, and G.P. Willeke. Progress in laser chemical processing (lcp) for innovative solar cell microstructuring and wafering applications. 2007.
- [22] D. Kray, A. Fell, S. Hopman, K. Mayer, S. W. Glunz, and G. P. Willeke. Laser chemical processing (lcp).a versatile tool for microstructuring applications. *Applied Physics A*, 93(1):99–103, 2008.
- [23] Tuan Anh Mai, Bernold Richerzhagen, Paul C. Snowdon, David Wood, and Paul G. Maropoulos. The laser microjet (lmj): a multi-solution technology for high quality micro-machining. volume 6459, page 64590P. SPIE, 2007.
- [24] K. Mayer. *Chemische Ansätze zur Neuordnung des Solarzellenprozesses ausgehend vom Wafering bis hin zur Emitterdiffusion*. PhD thesis, Johann Wolfgang Goethe - Universität, 2009.
- [25] Henning Nagel, Christopher Berge, and Armin G. Aberle. Generalized analysis of quasi-steady-state and quasi-transient measurements of carrier lifetimes in semiconductors. *Journal of Applied Physics*, 86(11):6218–6221, 1999.
- [26] H. Plagwitz, M. Schaper, J. Schmidt, B. Terheiden, and R. Brendel. Analytical model for the optimization of locally contacted solar cells. In *Photovoltaic Specialists Conference, 2005. Conference Record of the Thirty-first IEEE*, pages 999 – 1002, 2005.
- [27] B. Richerzhagen. *Entwicklung und Konstruktion eines Systems zur Uebertragung von Laserenergie für die Laserzahnbehandlung*. Dissertation, Ecole Polytechnique Fédérale de Lausanne, 1994.
- [28] B. Richerzhagen. Device for machining material with a laser, 2003.
- [29] Pierre Saint-Cast, Marc Rudiger, Andreas Wolf, Marc Hofmann, Jochen Rentsch, and Ralf Preu. Advanced analytical model for the effective recombination velocity of locally contacted surfaces. *Journal of Applied Physics*, 108(1):013705, 2010.
- [30] Oliver Schultz. High-efficiency multicrystalline silicon solar cells. 2005.
- [31] W. Shockley and W. T. Read. Statistics of the recombinations of holes and electrons. *Phys. Rev.*, 87(5):835–842, Sep 1952.
- [32] R.A. Sinton, A. Cuevas, and M. Stuckings. Quasi-steady-state photoconductance, a new method for solar cell material and device characterization. In

Bibliography

Photovoltaic Specialists Conference, 1996., Conference Record of the Twenty Fifth IEEE, pages 457 –460, May 1996.

- [33] Ronald A. Sinton and Andres Cuevas. Contactless determination of current-voltage characteristics and minority carrier lifetimes in semiconductors from quasi-steady-state photoconductance data. *Applied Physics Letters*, 69(17):2510 –2512, October 1996.
- [34] S.M. Sze and K.K. Ng. *Physics of semiconductor devices*. Wiley-Interscience publication. Wiley-Interscience, 2007.
- [35] North AU) Green Martin A. (Waverley AU) Wenham, Stuart R. (Bexley. Buried contact solar cell, February 1988.

Appendix A: LEE laser optical losses and pulse duration

In the following table, measured data for pulse duration and output power are summarized for LEE laser. *InternalL_{pow}* is the power measured at the plane before the optical fiber, while *L_{pow}* is measured at the fiber exit plane.

$\Delta\tau_{pulse}$ [ns]	<i>InternalL_{pow}</i> [W]	<i>L_{pow}</i> [W]
440.0	20.00	18.30
480.0	30.00	27.00
324.0	40.00	38.20
304.0	50.00	47.50
284.0	60.00	54.50
272.0	64.80	60.30

(a) @50kHz repetition rate

$\Delta\tau_{pulse}$ [ns]	<i>InternalL_{pow}</i> [W]	<i>L_{pow}</i> [W]
314.00	20.00	19.50
294.00	30.00	28.36
174.00	40.00	37.70
147.00	50.00	46.20
122.00	60.00	54.80
108.00	77.70	69.30

(b) @15kHz repetition rate

Table 5.0.1: LEE absorption and pulse duration data for different pulse repetition rates

Appendix B: Deep spots at the groove beginning

During the experimental work, a practical problem had to be faced. At the beginning of any processed groove, a spot deeper than the groove depth could be observed.

The explanation to this fact was found to be related to the axis moving in the machine. The *chuck*, that is, the part of the machine which holds the sample by means of a vacuum pump, provides the wafer with the necessary movement. When it starts to move to allow the wafer surface to be scanned by the optical head, its velocity is not yet constant. An acceleration ramp is set, which duration is unknown. During the ramp, the scanning speed is lower than the nominal value, thus causing a higher pulse overlap.

This affects the begin of the groove with deep spots, that in some cases become also passing-through holes.

The identified solution was to find a way to delay the laser emission during the chuck acceleration ramp. This was differently achieved for the two machines (LCS and R&D). In R&D the CNC program that was used contained already some instructions to set the delay up. For LCS processing, instead, an external delayer was introduced in the line between the machine and the laser. In this way, the laser shutter opening was no more controlled by the coupling machine but directly by the delayer. By setting suitable delays, the wanted periodical rectangular function for the shutter opening and closing was reconstructed.

The results obtained after these correction were no more affected by the deep spots.

Appendix C: supplement to Chapter 3

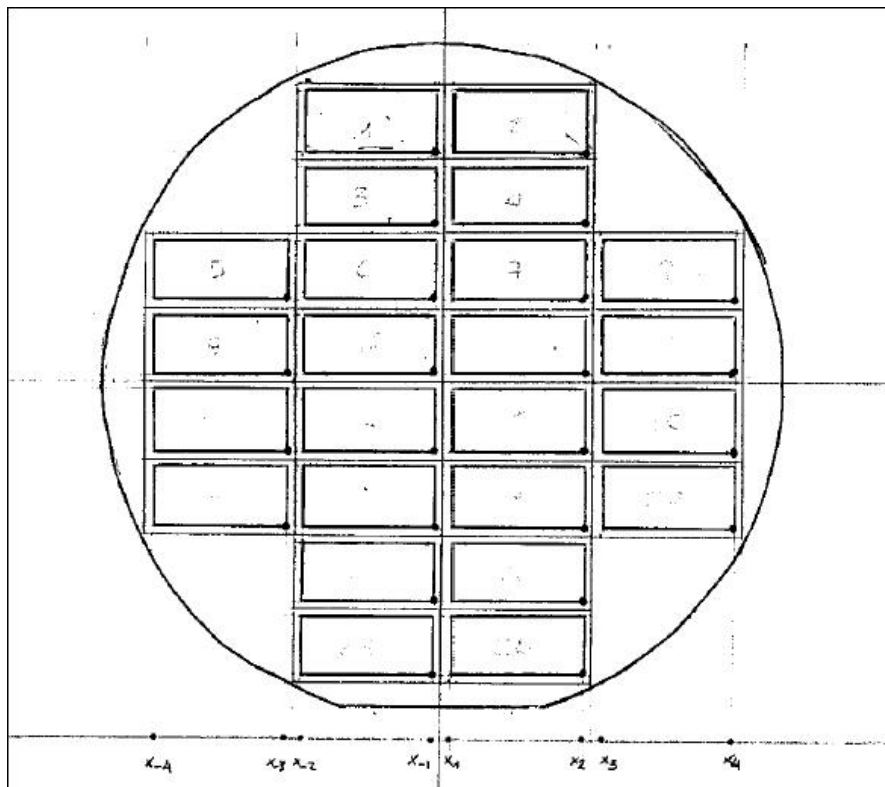


Figure 5.0.1: Sketch of a processed wafer with 24 fields

Appendix D: Supplement to Chapter 4

Here is a table showing the parameters used for the processing on Cz-boron doped wafers, SiO₂ passivated on both sides. The pulse energy has been varied in a wide range (covering the whole allowed range for HIPPO) and the pitch was fixed for all the processed fields.

Laser system	Nozzle diameter	Press	Freq	L_{pow}	E_p	Ssp
HIPPO/LEE	[μm]	[bar]	[kHz]	[W]	[mJ]	[mm/s]
HIPPO	50	100	35	2	0,057	25
				3	0,086	30
				4	0,114	30
				5	0,143	35
				6	0,171	40
HIPPO	50	160	35	1	0,029	10
				2	0,057	20
				3	0,086	30
				4	0,114	35
				5	0,143	400
				6	0,171	45
LEE	50	160	50	4,53	0,091	40
				9,18	0,184	60
				13,84	0,277	100

Table 5.0.2: First parameters used for QSSPC measuring

Aknowledgments

I would like to express my gratitude to Prof. Li Bassi and Ph.D. Andreas Fell for supervising this collaborative work, as well as to Ph.D. Filip Granek in his position of groupleader at Fraunhofer ISE.

The knowledge and experience shared by the whole MLV group at Fraunhofer ISE has been a great opportunity for me to learn not only specific notions and methods, but also a general attitude towards research. I thank them all.

I am grateful to Andreas Fell, whose knowledge and guiding have been invaluable, for being a supportive mentor encouraging me to develop my own ideas.

I thank the MLV groupleader Filip Granek, who has been overseeing my work, giving me precious advice and strong motivation.

Matthias Mesec's tutoring is also greatly appreciated, especially for the laboratory activity; his patience and helpfulness have been a reference point.

Thanks also to Sven Kluska and Christoph Fleischmann for fruitful discussions and knowledge-sharing, as well as Sybille Hopmann and Timur Knarozovskiy.

A special mention to other students in MLV, Marcin, Matthias B., Niklas, Stephanie, Phillip, Mihai and Matthias W., who have been cheerful mates in this adventure.

Some staff and students outside the MLV at Fraunhofer ISE have also contributed to this work, and I am grateful in particular to Antonio Leimenstoll and Felix Schaetzle.

I am grateful to the city of Freiburg for its being so lovely and their inhabitants for the warm welcome I received.

My friends' support has been fundamental, being goad and embrace at the same time. I thank my German friends all, for they always make me feel home. Thanks to Elena, Federico and Aria; I was never alone.

Last but not least, I express my deepest thankfulness to my family and my beloved Alberto who are always encouraging me to fulfil my goals, even if they take me away from them. Their love has been my strength.

Thanks to my father, who taught me never to give up.